MIT Open Access Articles

Early diagenesis of sulfur in Bornholm Basin sediments: The role of upward diffusion of isotopically "heavy" sulfide

The MIT Faculty has made this article openly available. ***Please share*** how this access benefits you. Your story matters.

Citation	Liu, Jiarui, Pellerin, André, Antler, Gilad, Izon, Gareth, Findlay, Alyssa J. et al. 2021. "Early diagenesis of sulfur in Bornholm Basin sediments: The role of upward diffusion of isotopically "heavy" sulfide." Geochimica et Cosmochimica Acta, 313.
As Published	10.1016/j.gca.2021.08.018
Publisher	Elsevier BV
Version	Final published version
Citable link	https://hdl.handle.net/1721.1/138293
Terms of Use	Creative Commons Attribution 4.0 International license
Detailed Terms	https://creativecommons.org/licenses/by/4.0/

Massachusetts Institute of Technology

DSpace@MIT

Available online at www.sciencedirect.com

ScienceDirect

Geochimica et Cosmochimica Acta 313 (2021) 359–377

Geochimica et Cosmochimica Acta

www.elsevier.com/locate/gca

Early diagenesis of sulfur in Bornholm Basin sediments: The role of upward diffusion of isotopically "heavy" sulfide

Jiarui Liu [a,b,*], André Pellerin [a,c], Gilad Antler [d,e], Gareth Izon [f], Alyssa J. Findlay [a], Hans Røy [a], Shuhei Ono [f], Sabine Kasten [g,h], Alexandra V. Turchyn [i], Bo Barker Jørgensen [a]

[a] *Section for Microbiology, Department of Biology, Aarhus University, 8000 Aarhus C, Denmark*
[b] *Department of Earth, Planetary and Space Sciences, University of California, Los Angeles, CA 90095, USA*
[c] *Institut des sciences de la mer de Rimouski, Rimouski, Québec G5L 3A1, Canada*
[d] *Department of Earth and Environmental Sciences, Ben-Gurion University of the Negev, Beersheba 84105, Israel*
[e] *The Interuniversity Institute for Marine Sciences, Eilat 88103, Israel*
[f] *Department of Earth, Atmospheric and Planetary Sciences, Massachusetts Institute of Technology, Cambridge, MA 02139, USA*
[g] *Alfred Wegener Institute Helmholtz Centre for Polar and Marine Research, 27570 Bremerhaven, Germany*
[h] *Faculty of Geosciences, University of Bremen, 28359 Bremen, Germany*
[i] *Department of Earth Sciences, University of Cambridge, Cambridge CB2 3EQ, UK*

Received 8 March 2021; accepted in revised form 17 August 2021; available online 25 August 2021

Abstract

Sediment-hosted marine sulfur cycling has played a significant role in regulating Earth's surface chemistry over our planet's history. Microbially-mediated reactions involving sulfur are often accompanied by sulfur isotope fractionation that, in turn, is captured by sulfate and sulfide minerals, providing the opportunity to track changes in the microbial utilization of sulfur and thus the marine sulfur cycle. Studying sulfur diagenesis within the Bornholm Basin, Baltic Sea, we explore the interplay between carbon, sulfur and iron, focusing on the fate of sulfur and the dynamics of the sulfur and oxygen isotopic response as a function of the varying thickness of the organic carbon-rich Holocene Mud Layer (HML) across the basin. Using a one-dimensional reaction-transport model, porewater sulfate and sulfide profiles were used to calculate net sulfate reduction rates (SRR) and net sulfide production rates, respectively. These calculations suggest a positive relationship between the thickness of the HML and net rates of sulfate reduction and sulfide production. Given that ascending sulfide is enriched in ^{34}S relative to that produced *in-situ*, a heightened sulfide flux promotes spatially variable precipitation of ^{34}S-enriched pyrite ($\delta^{34}S \approx -10‰$) close to the sediment–water interface. Modeling results indicate that this isotopically "heavy" sulfide is formed as a consequence of mixing between ascending sulfide (up to +6.3‰) and that produced *in-situ* (ca. −40‰). Further, we show that the sulfur and oxygen isotopic composition of porewater sulfate is controlled by the net SRR: when the net SRR is high (i.e., in sulfide-replete settings) the downcore increase in $\delta^{18}O_{SO4}$ is dampened relative to increase in $\delta^{34}S_{SO4}$, whereas when net SRR is low (i.e., in iron-rich parts of the basin) downcore $\delta^{18}O_{SO4}$ values increase while $\delta^{34}S_{SO4}$ values remain invariant. We conclude that sedimentation rates and open system diffusion strongly influence the distribution of sulfur species and their sulfur isotopic composition, as well as the oxygen isotopic composition of sulfate, through the interaction between iron, sulfur

* Corresponding author at: Department of Earth, Planetary and Space Sciences, University of California, Los Angeles, CA 90095, USA. *E-mail address:* jiaruiliu@ucla.edu (J. Liu).

https://doi.org/10.1016/j.gca.2021.08.018
0016-7037/© 2021 The Author(s). Published by Elsevier Ltd.
This is an open access article under the CC BY license (http://creativecommons.org/licenses/by/4.0/).

and methane. This work highlights the importance of considering diffusion to better understand open system diagenesis and the $\delta^{34}S$ signatures of sulfate and sulfide in both modern settings and ancient rocks.
© 2021 The Author(s). Published by Elsevier Ltd. This is an open access article under the CC BY license (http://creativecommons.org/licenses/by/4.0/).

Keywords: Baltic Sea; Biogeochemical sulfur cycle; Marine sediments; Multiple sulfur isotopes; Oxygen isotopes of sulfate; Pyrite

1. INTRODUCTION

Biogeochemical sulfur cycling in marine sediments is driven by microbial sulfate reduction that, through its intrinsic links with other bio-essential elemental cycles, affects Earth's surface oxidation state on geologically-relevant timescales (e.g., Jørgensen and Kasten, 2006; Fike et al., 2015). Following the consumption of oxygen in shallow sediments, dissimilatory sulfate reduction represents the principal means of anaerobic organic matter mineralization (Jørgensen, 1982). The reduction of sulfate can be coupled to the oxidation of organic matter that is deposited on the seafloor, commonly referred to as organoclastic sulfate reduction (OSR). Sulfate reduction can also be coupled to the anaerobic oxidation of methane (AOM; e.g., Niewöhner et al., 1998; Knittel and Boetius, 2009; Egger et al., 2018). Both processes serve as a source of aqueous sulfide to sedimentary porewater. Whilst most of this microbially-generated sulfide is re-oxidized to sulfate, a fraction precipitates with reactive iron within the sediment, ultimately forming pyrite (Berner, 1970, 1984; Hensen et al., 2003; Jørgensen and Nelson, 2004). Given that microbially-induced redox transformations between sulfur-bearing species are frequently accompanied by readily measurable stable isotope fractionations (e.g., Kaplan and Rittenberg, 1964; Canfield and Thamdrup, 1994; Canfield, 2001; Pellerin et al., 2015), the distributions of sulfur's two most abundant stable isotopes (^{32}S and ^{34}S, expressed as $\delta^{34}S$) in sulfur-bearing minerals have been widely adopted as a geochemical tool, informing on contemporary diagenesis and, more widely, on the operation of the sulfur cycle throughout Earth history (e.g., Kaplan et al., 1963; Strauss, 1997; Jørgensen et al., 2004; Bottrell and Newton, 2006; Fike et al., 2015).

Sulfate-reducing microorganisms preferentially reduce $^{32}SO_4^{2-}$ over its ^{34}S-containing isotopologue, imparting an up-to-70‰ ^{34}S-depletion in the resultant sulfide under appropriate conditions (Wortmann et al., 2001; Brunner and Bernasconi, 2005; Sim et al., 2011a). The cell-specific sulfate reduction rate (csSRR) controls the magnitude of this sulfur isotope fractionation, with culture experiments demonstrating that an increased csSRR yields lower sulfur isotope fractionation (Kaplan and Rittenberg, 1964; Sim et al., 2011b; Leavitt et al., 2013). It follows that the generally low availability and high recalcitrance of metabolizable substrates in marine sediments result in low csSRR, fostering the expression of large, and generally constant, sulfur isotope fractionation (i.e., ca. 70‰; Hoehler and Jørgensen, 2013; Wing and Halevy, 2014; Masterson et al., 2018; Jørgensen et al., 2019b). The sulfate-pyrite $\delta^{34}S$ offset, however, is highly variable in nature, reflecting the dynamics of sulfate and sulfide transport and reaction within marine sedimentary pore fluids, as well as diffusive and advective exchange with overlying seawater (e.g., Canfield, 2001; Jørgensen et al., 2019b). Put differently, stratigraphic variation observed in pyrite $\delta^{34}S$ values is strongly controlled by local environmental, depositional and diagenetic processes, including the content and reactivity of organic matter, ambient sulfate concentration, availability of reactive iron minerals, sedimentation rate, porosity, sedimentary reworking, bioturbation, and prevailing bottom-water oxygen concentrations amongst a myriad of other interconnected factors (Berner, 1984; Middelburg, 1991; Kasten et al., 1998; Wijsman et al., 2001; Aller et al., 2010; Fike et al., 2015; Gomes and Hurtgen, 2015; Pasquier et al., 2017, 2021; Shawar et al., 2018; Liu et al., 2019; Lang et al., 2020; Liu et al., 2021). In certain environments (e.g., methane seeps), the sulfur isotope fractionation and sulfate-pyrite $\delta^{34}S$ offset can be smaller due to higher substrate concentration (e.g., Deusner et al., 2014; Gong et al., 2018). Once formed, pyrite is stable in anoxic conditions and accumulates within the sediment column where it may be progressively overprinted by subsequent diagenetic processes. Thus, the $\delta^{34}S$ of a depth-specific bulk sedimentary pyrite pool (i.e., that quantified via chemical extraction) is the product of cumulative diagenesis, implying that time affects the abundance and isotopic composition of subsurface pyrite (Lin et al., 2016; Riedinger et al., 2017; Liu et al., 2020b).

Importantly, sediments are open to diffusion of sulfate and sulfide in the pore fluids, which influences their $\delta^{34}S$ values (Jørgensen, 1979; Goldhaber and Kaplan, 1980; Chanton et al., 1987; Jørgensen et al., 2004). Since microbial sulfate reduction progressively enriches ^{34}S in the residual porewater sulfate and in the subsequently formed sulfide, the diffusion gradients of ^{32}S and ^{34}S differ from their relative concentrations in the bulk sulfate and sulfide (Jørgensen, 1979; Jørgensen et al., 2004). For example, due to the gradual increase in $\delta^{34}S$ of sulfide with depth, the $H_2^{32}S$ gradient is relatively less steep than the $H_2^{34}S$ gradient, meaning that $H_2^{34}S$ has a relatively higher flux than $H_2^{32}S$. Any ascending (upward) sulfide flux will therefore be ^{34}S-enriched relative to the sulfide pool at any given depth. The opposite is true for the descending (downward) diffusive sulfate flux, which is relatively enriched in ^{32}S (Jørgensen, 1979; Jørgensen et al., 2004). Despite being a well-documented effect in sulfur isotope geochemistry of sediments, it remains unclear to what extent this open system diffusion explains the shallow precipitation of ^{34}S-enriched pyrite.

The $\delta^{34}S$ values of pyrite are indeed highly variable near the sediment–water interface, for example, ranging from −45‰ in a continental slope setting (e.g., Lin et al., 2016) to −28‰ in a continental shelf setting (e.g., Liu et al., 2020a) where large sulfur isotope fractionations are

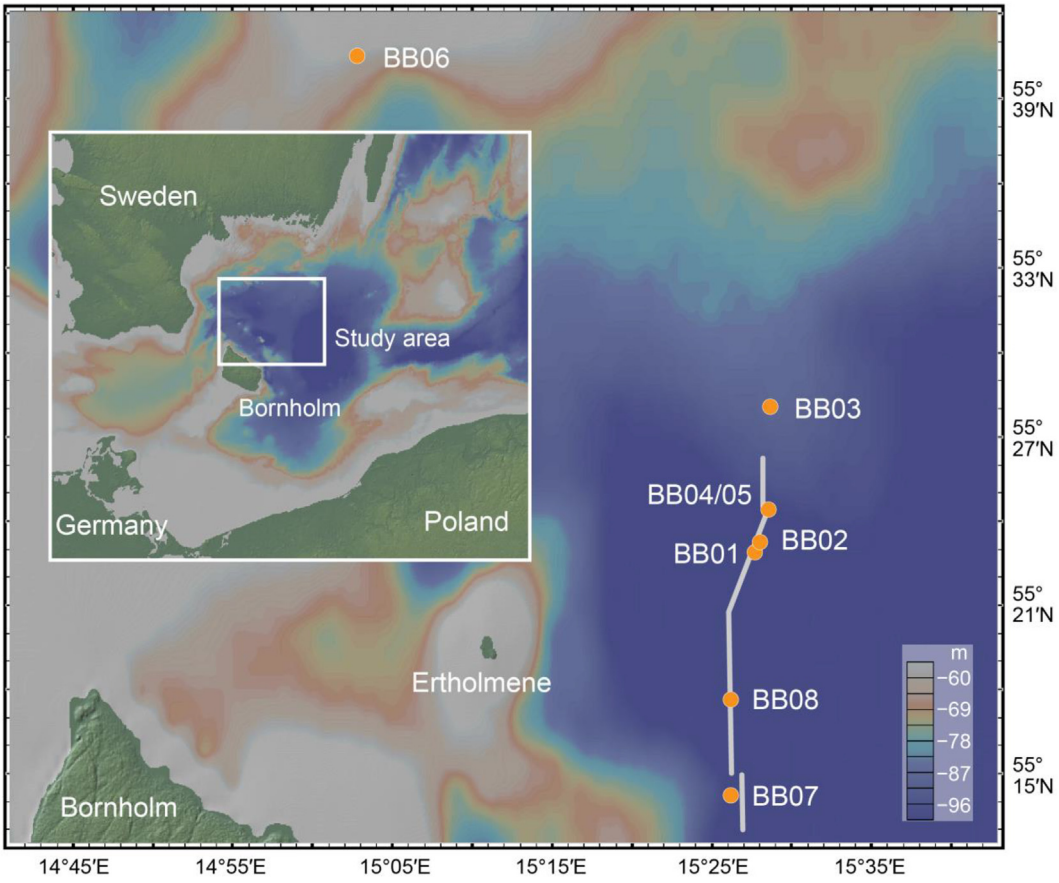

Fig. 1. A bathymetric map locating the study sites (orange circles) along seismo-acoustic transects (grey lines; Fig. 2a) within the Bornholm Basin. Here, the insert places the enlargement (white box) within the wider southwestern Baltic Sea. This figure was generated using GeoMapApp (http://www.geomapapp.org/).

expected due to the low csSRR. To the best of our knowledge, there is no conclusive evidence to explain this discrepancy between the expected sulfur isotope fractionation and the measured sulfur isotopic composition of near-surface pyrite. To examine this knowledge gap, we leverage a suite of cores from the Bornholm Basin in the southwest Baltic Sea (Fig. 1). Augmenting existing data from cores BB01–BB05 (Liu et al., 2020a, 2021), we here report sulfur concentrations and isotopic data from an additional three sediment cores (BB06, BB07 and BB08). In combination, these cores comprise a basin-wide transect with differential subsurface sulfide fluxes designed to test the hypothesized importance of an ascending diffusive flux of ^{34}S-enriched sulfide on the δ^{34}S budget of near-surface pyrite.

2. MATERIALS AND METHODS

2.1. Site description

The 75–99 m deep Bornholm Basin is located in the southwestern Baltic Sea (Fig. 1). Here, the sedimentary succession shifts from light-brown clay at depth to dark-grey Holocene-aged mud in its upper reaches. This distinctive lithological transition at depths varying between 0.1 and 20.7 mbsf (meter below seafloor; Table 1, Fig. 2a) archives a glacial–interglacial sedimentary overhaul, capturing the post-glacial marine transgression, which fueled the deposition of the organic-rich, sulfidic Holocene Mud Layer (HML) that succeeded the pre-existing organic-lean and iron-rich lacustrine clays (Andrén et al., 2000; Sohlenius et al., 2001; Jensen et al., 2017). These lacustrine sediments overlie bedrock-hosted glacial tills deposited during the last glaciation and record various freshwater/brackish stages of the Baltic Sea's evolution (i.e., from the Baltic Ice Lake to the Yoldia Sea and Ancylus Lake, Fig. 2a; Andrén et al., 2000; Moros et al., 2002). At ca. 8.5 ka BP, the brackish-marine Littorina Sea mud started to accumulate, however the underlying fault-controlled and glaciogenic topography induced distinct spatial variability in the thickness of the HML (Table 1, Fig. 2a; Jensen et al., 2017; Hilligsøe et al., 2018). Nevertheless, at any given location, based on ^{14}C dates of shells, seismo-acoustic markers and biostratigraphic markers, these Holocene-aged marine sediments accumulated at a roughly constant rate (Andrén et al., 2000; Jensen et al., 2017; Beulig et al., 2018). The total organic carbon contents are more or less invariant in the HML (4.9 ± 0.7 wt%, 1σ) and drop sharply to 0.6 ± 0.1 wt% (1σ) in the deep lacustrine clay deposits (Beulig et al., 2018).

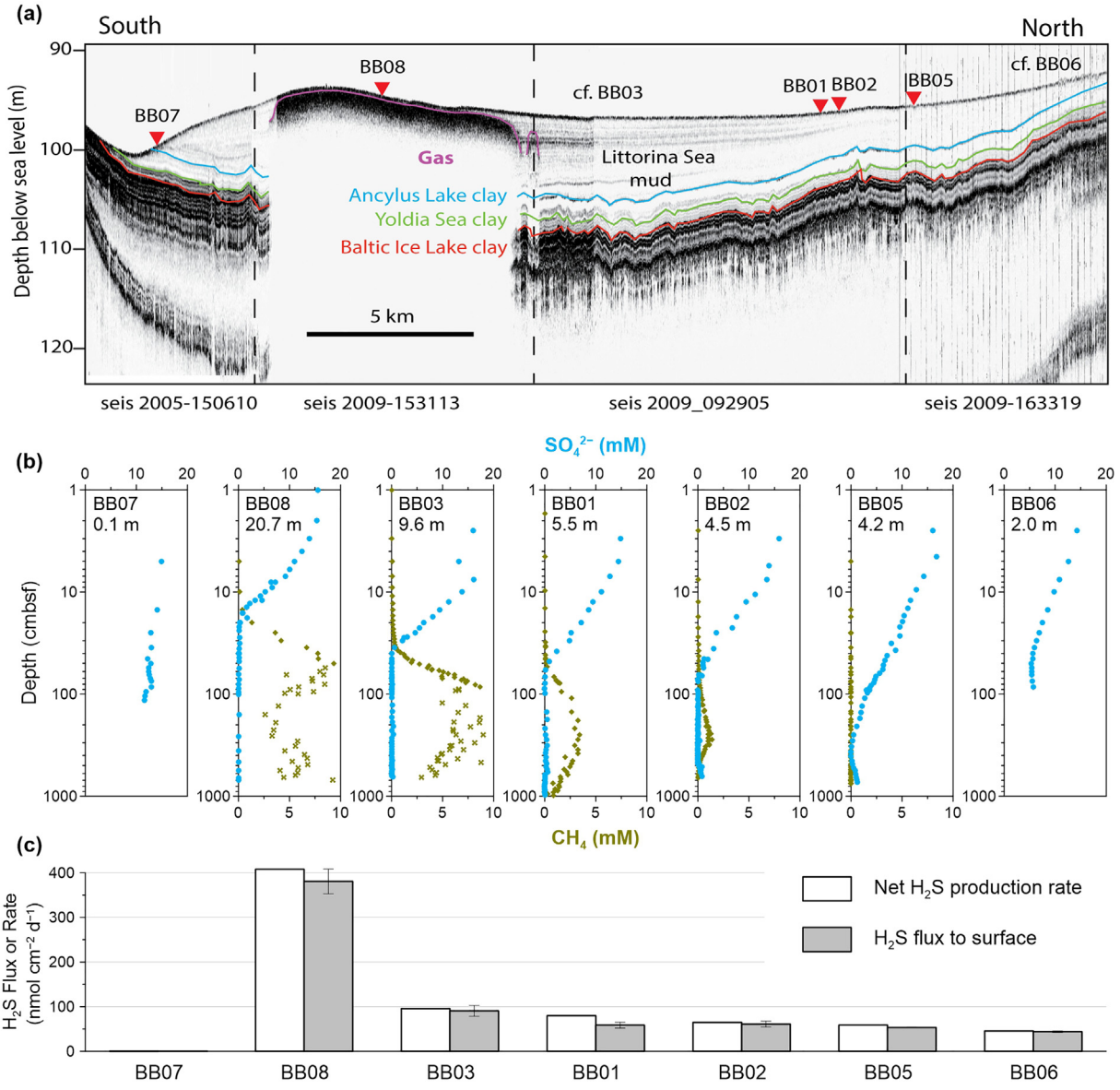

Fig. 2. (a) A stratigraphically annotated N–S seismic transect spanning the Bornholm Basin (from Hilligsøe et al., 2018). Methane bubbles present within the shallow sub-surface are responsible for the observed near-surface acoustic blanking. Sample sites are located by red triangles, while off-transect sites (BB03 and BB06) are placed on the transect according to the thickness of the Holocene Mud Layer (HML). (b) Spatially arranged downcore porewater sulfate (blue circles) and methane (olive diamonds) concentration profiles. The HML thickness is shown for each site. Methane concentration data from the deeper parts of sites BB08 and BB03 have been compromised by outgassing and are distinguished from the shallower, non-compromised data by a separate symbol (olive crosses). Note the logarithmic depth scale. (c) Site-specific depth-integrated net sulfide production rates (white) and upward sulfide fluxes (grey). Error bars denote 1σ uncertainties. Data from this study (sites BB06–BB08) are augmented by data from Beulig et al. (2018), Hilligsøe et al. (2018) and Liu et al. (2020a, 2021).

Within the Bornholm Basin, sediment cores were taken at eight stations during a research cruise in 2016 on the R/V *Aurora* (Fig. 1). Guided by preceding exploratory cruises, the study sites were selected according to their organic matter burial histories and the thickness of the HML (Table 1). Site BB08 represents a reoccupation of site 374190 sampled during R/V *Poseidon* Expedition PO392 in 2009 (Hilligsøe et al., 2018). Coring included gravity (~9 m in length), Rumohr (~1 m in length) and Haps (~25 cm in length) corers. An Innomar sediment echo sounder (10 kHz) was used to generate a seismo-acoustic transect joining the cored sites, while disclosing the stratigraphic structure of the Bornholm Basin (Hilligsøe et al., 2018). At sites BB01–BB08, with the exception of porewater sulfate $\delta^{18}O$ data, porewater and solid-phase data from sites BB01–BB05 have been published (Beulig et al., 2018; Pellerin et al., 2018; Liu et al., 2020a, 2021). These data are augmented with those from sites BB06–BB08 that are reported for the first time herein.

Table 1
Details describing the sampling sites within the Bornholm Basin. Here, sites have been arranged by the thickness of the Holocene Mud Layer (HML). ω denotes the sedimentation rate. SMT, mbsf and ka abbreviate sulfate–methane transition, meter below seafloor and kiloannum, respectively. Data from this study (sites BB06–BB08) are augmented by data from Beulig et al. (2018) and Liu et al. (2020a, 2021). Site BB08 represents a reoccupation of site 374190, and its HML thickness was reported by Hilligsøe et al. (2018).

Site	Latitude/longitude	Water depth (m)	HML thickness (m)	ω (cm ka^{-1})	SMT depth (mbsf)
BB08	55°17.663′N/15°26.201′E	91	20.7	244	0.2
BB03	55°28.119′N/15°28.647′E	84	9.6	113	0.4
BB01	55°22.922′N/15°27.675′E	96	5.5	65	0.6
BB02	55°23.281′N/15°28.004′E	96	4.5	53	0.7
BB04	55°24.094′N/15°28.397′E	95	4.2	49	3.7
BB05	55°24.418′N/15°28.550′E	95	4.2	49	3.7
BB06	55°40.500′N/15°02.754′E	75	*ca.* 2.0	*ca.* 24	No SMT
BB07	55°14.249′N/15°26.198′E	99	0.1	1	No SMT

2.2. Porewater sampling and analyses

The sampling and analytical procedures follow those described by Beulig et al. (2018), Pellerin et al. (2018) and Liu et al. (2020a). Briefly, sediments for methane analysis were collected through small holes drilled in the core liner, transferred to gas-tight glass vials containing a saturated NaCl solution and capped immediately after core retrieval. After gas equilibration, headspace methane concentrations were quantified by gas chromatography using an SRI 310C GC equipped with a packed silica gel column and a flame ionization detector. The detection limit was $\leq$1 μM of porewater CH_4. Porewater sampling was achieved using Rhizon soil moisture samplers inserted directly into the cores and connected to Vacutainers®. Dissolved sulfide was stripped from designated porewater samples using humidified CO_2, allowing sulfate concentrations to be determined by ion chromatography in a Dionex system following elution in KOH from an AG-18/AS-18 column. Aqueous sulfide (ΣH_2S) was fixed using 5% zinc acetate solution and frozen, allowing subsequent sulfide concentrations to be quantified spectrophotometrically (Cline, 1969) with a detection limit of $\leq$1 μM porewater sulfide. Dissolved iron was determined by inductively coupled plasma mass spectrometry (ICP-MS) following dilution with 0.01 N HNO_3 using a Thermo Fisher Scientific Element 2 ICP-MS. The analytical uncertainties associated with porewater methane, sulfate, sulfide and iron concentrations were determined by replicate analysis of standards, which all displayed relative standard deviations (RSD) of better than 3–5%.

2.3. Solid-phase sediment sampling and analyses

Plunge samples were taken using cutoff syringes through windows cut in the core liner, sealed with Parafilm® and frozen at −20 °C under anoxic conditions. Frozen sediment samples were transferred to glass vials containing sufficient 5% zinc acetate solution to submerge each sample. Zero-valent sulfur (ZVS, mainly elemental sulfur) was then extracted from defrosted sediments via sustained agitation in a 3:1 methanol:toluene mixture for ~15 hours. Dissolved ZVS was quantified at 230 nm by a UV detector following reversed-phase high-performance liquid chromatographic separation over a C-18 column and elution in 98:2 methanol:water (Findlay et al., 2014).

The supernatant and the sediment residue were transferred to separate round-bottom flasks for conversion to sulfide for mass spectrometric analysis: First the ZVS was converted to sulfide upon treatment with chromium(II), while the separated solid residue was extracted sequentially with 6 N HCl to release acid volatile sulfur (AVS, mainly Fe monosulfides) and then with chromium(II) to release the chromium reducible sulfur (CRS, mainly pyrite; Fossing and Jørgensen, 1989). These solid-phase sulfur species were captured in 5% zinc acetate traps and the AVS and CRS contents were determined spectrophotometrically (Cline, 1969). Finally, sulfide from ZVS, AVS and CRS was converted from ZnS to Ag_2S via addition of silver nitrate and ammonium hydroxide.

2.4. Stable sulfur and oxygen isotope analyses

Porewater sulfide was converted from ZnS to Ag_2S, while porewater sulfate was precipitated as barite ($BaSO_4$). This barite was subsequently cleaned with 6 N HCl and twice with deionized water. The precipitated Ag_2S from porewater sulfide, ZVS, AVS and CRS was rinsed with deionized water. Once cleaned and dried, these precipitates were combusted at 1030 °C using a Flash Element Analyzer. The sulfur isotopic composition of the resulting SO_2 was determined by continuous-flow gas-source isotope-ratio mass spectrometry (GS-IRMS) using a Thermo Finnegan Delta V Plus at the Godwin Laboratory of the University of Cambridge. Multiple sulfur isotope data was obtained by fluorination of 2–3 mg aliquots of homogenized Ag_2S (Ono et al., 2012). Briefly, sulfur was converted from a solid- to gas-phase (SF_6) analyte via overnight reaction beneath a 100 Torr F_2 atmosphere at 300 °C. Following automated cryogenic and gas chromatographic separation, the purified SF_6 was transferred into a vacant multi-port on a designated Thermo MAT 253 IRMS operated in dual-inlet mode in the Laboratory of Stable Isotope Geobiology at the Massachusetts Institute of Technology.

Sulfur isotopic data are reported in standard delta-notation (Eq. (1)):

$$\delta^{3X}S\ (‰) = \left[\left({}^{3X}R_{Sample}/\ {}^{3X}R_{VCDT}\right) - 1\right] \times 1000 \quad (1)$$

where ${}^{3X}R_{Sample}/{}^{3X}R_{VCDT}$ is the sulfur isotopic ratio of a sample (${}^{3X}R_{Sample} = {}^{3X}S/{}^{32}S$ and 3X = 33 or 34) relative to Vienna Canyon Diablo Troilite (VCDT). The minor sulfur isotopic composition is presented in $\Delta^{33}S$ notation (Eq. (2)):

$$\Delta^{33}S\ (‰) = \delta^{33}S - 1000 \times \left[\left(1 + \frac{\delta^{34}S}{1000}\right)^{0.515} - 1\right] \quad (2)$$

Analyses of $\delta^{34}S$ were normalized to VCDT using standards distributed by the International Atomic Energy Agency (IAEA S1, S2, S3) and the National Bureau of Standards (NBS127) as well as in-house standards. The analytical uncertainty associated with SF_6 measurements was determined to be 0.2‰ and 0.005‰ (1σ) for $\delta^{34}S$ and $\Delta^{33}S$, respectively; while measurements using SO_2 had $\delta^{34}S$ uncertainties of 0.3‰ (1σ).

For the analysis of $\delta^{18}O_{SO4}$, barite was pyrolyzed at 1450 °C in a Temperature Conversion Element Analyzer (TC/EA), producing carbon monoxide. The oxygen isotopic composition of the resulting carbon monoxide was determined by continuous-flow GS-IRMS using a Thermo Finnegan Delta V Plus at the Godwin Laboratory of the University of Cambridge. Analyses of $\delta^{18}O_{SO4}$ were conducted in triplicate and normalized to Vienna Standard Mean Ocean Water (VSMOW) using NBS 127, IAEA-SO-5, and IAEA-SO-6. The $\delta^{18}O_{SO4}$ uncertainty of these replicate analyses was 0.3‰ (1σ).

2.5. Diffusive flux and modeling of sulfide and sulfate

Vertical diffusive fluxes (*J*) of porewater sulfide were calculated using Fick's First Law (Eq. (3)):

$$J = -\varphi \times Ds \times \frac{\partial C}{\partial z} \quad (3)$$

where φ is sediment porosity, *Ds* is the sediment diffusion coefficient of the solute, *C* is its concentration in pore fluids, and *z* is the depth below the seafloor. The vertical concentration gradient (*dC/dz*) was approximated via linear regression of the ΣH_2S concentration right below the sediment surface (e.g., down to 15 cmbsf). Using the molecular diffusion coefficient (*D*) and measured porosity, *Ds* was calculated using the empirical equation (Eq. (4)) to compensate for tortuosity (e.g., Iversen and Jørgensen, 1993):

$$Ds = D/(1 + 3(1 - \varphi)) \quad (4)$$

The respective pH, salinity and temperature of the Bornholm surface sediments were found to be 8.0, 17 and 9 °C (Hilligsøe et al., 2018), equating to a H_2S:HS^- ratio of 1:15 (Millero et al., 1988). In natural settings the contribution of S^{2-} is relevant only in hyperalkaline settings (pH > 14) and hence has been ignored here (Millero et al., 1988). Using an *in-situ* sediment temperature of 9 °C, calculated respective HS^- and H_2S diffusion coefficients were 1.037 and 1.123 $cm^2\ d^{-1}$, yielding an effective diffusion coefficient (*D*) for ΣH_2S of 1.042 $cm^2\ d^{-1}$ (Jørgensen et al., 2004). Here, when the units of *C* are μM, the resulting flux, *J*, is expressed in nmol $cm^{-2}\ d^{-1}$.

Different approaches were used to quantify and compare the processes occurring in the sediments across the basin. Sulfate reduction rates (SRR) were determined experimentally using ^{35}S-labeled sulfate (Beulig et al., 2018). Here, the depth-integrated rate represents the gross SRR throughout the sediment column. This directly-measured gross SRR most closely approximates the total rate of sulfate reduction in the sediment (Jørgensen et al., 2004). The net SRR derived from modeling of dissolved sulfate porewater gradients represents the gross SRR minus the concurrent re-oxidation of reduced sulfur species back to sulfate (Jørgensen et al., 2004). The net sulfide production rate derived from modeled porewater H_2S gradients represents a measure of the net SRR minus H_2S loss by either metal sulfide precipitation or organic matter sulfidization (Jørgensen et al., 2004). At steady state, and given the relatively low sedimentation rate (<3 m ka^{-1}; Table 1), the net sulfide production rate is equivalent to the sum of the upward and downward fluxes of H_2S.

To calculate the rates of net sulfate reduction and net sulfide production, we performed one-dimensional reaction-transport modeling using the software, PROFILE (Berg et al., 1998). Assuming that the depth profiles of sulfate and sulfide concentration reflect a quasi-steady state, the PROFILE model divided the sediment pile into several discrete depth intervals (e.g., 1–4 zones; Berg et al., 1998), each with a constant process rate, which optimally reproduced the measured concentration profiles. Here, transport is exclusively assumed to occur via molecular diffusion—a criterion that we deem realistic in the deep Bornholm Basin where the bottom water is generally hypoxic–anoxic, limiting bioirrigation and bioturbation, and the uppermost sediments are devoid of gas bubbles (Carstensen et al., 2014; Hilligsøe et al., 2018). Porewater sulfate concentrations at the top and the bottom of the modeled depth interval were used as boundary conditions. Since several cores only penetrated the upper part of the sulfidic zone, measured sulfide concentrations and the upward fluxes near the top of the core were adopted as boundary conditions for modeling porewater sulfide profiles. The modeled volumetric rates are in units of nmol $cm^{-3}\ d^{-1}$, while the depth-integrated rates are reported in units of nmol $cm^{-2}\ d^{-1}$.

2.6. Model for sulfur isotopic composition of aqueous sulfide near the sediment surface

A mixing model was used to understand the near-surface $\delta^{34}S$ systematics of H_2S in the Bornholm Basin. The model was predicated on our observation that H_2S in the upper centimeters of the sediment has two sources: sulfide produced by *in-situ* microbial sulfate reduction (i.e., the measured gross SRR) and sulfide diffusing from below (i.e., the measured ascending sulfide flux). Both sources of sulfide underwent abiotic oxidation fueled primarily by Fe-oxides as well as potential microbially-mediated oxidation facilitated by sulfur-oxidizing bacteria (e.g., *Beggiatoaceae*) and cable bacteria (Hermans et al., 2019). Indeed, intense

sulfide oxidation near the sediment surface maintained H_2S concentrations below detection at most of the sites. Given that H_2S detection occurred at about 5 cm sediment depth on average across the examined cores, we take the upper 5 cm as one box for the model. Since 3 cmbsf was the shallowest depth where porewater sulfide $\delta^{34}S$ data were available at many of the study sites, this was adopted as the comparison depth to assess the model's performance.

Beulig et al. (2018) showed that the SRR in the upper centimeters is broadly the same among four sites (BB01–BB04) in the Bornholm Basin (86.6–97.9 nmol cm^{-2} d^{-1}, 0–5 cmbsf). Consequently, the rate of *in-situ* sulfide production ($Rate_{in\text{-}situ\ SR}$; gross production) was calculated by integration of the measured SRR across the upper 5 cm (91.9 ± 4.9 nmol cm^{-2} d^{-1}, 1σ), while the ascending sulfide flux ($J_{diffusion}$) was derived following Section 2.5. The lowest measured $\delta^{34}S$ in H_2S and pyrite was −40‰, representing the estimated $\delta^{34}S$ of the earliest pyrite precipitated at the sediment–water interface where *in-situ* sulfide production was the main sulfide source (e.g., site BB07). Thus, the sulfur isotope fractionation was assumed to be 63‰ with a $\delta^{34}S_{in\text{-}situ\ H2S}$ of −40‰, given that the average $\delta^{34}S$ of sulfate was 23‰ at 3 cmbsf. We consider this sulfur isotope fractionation (63‰) to be realistic for the Bornholm Basin because this is close to the maximum sulfur isotope fractionation observed in culture experiments (66‰; Sim et al., 2011a) and because the sediment properties, total organic carbon content, and SRR are broadly the same in the upper 5 cm among the study sites (Beulig et al., 2018; Hilligsøe et al., 2018).

Using the combined concentration and isotope data, the separate diffusion fluxes of $H_2^{32}S$ and $H_2^{34}S$ were calculated. At circumneutral pH it has been experimentally shown that the diffusion coefficients for the two most common H_2S isotopologues differ by less than 1%, resulting in a diffusion-induced isotope effect of ca. 0.4‰ in seawater (Piel, 1999; Jørgensen et al., 2004; Baune and Böttcher, 2010). Given that this approximates the uncertainty associated with the $\delta^{34}S$ determination (0.3‰), the diffusion coefficients (*Ds*) of the two isotopic species were assumed to be identical. The isotope fractionation is therefore not affected by a difference in diffusion coefficients (Baune and Böttcher, 2010; Wortmann and Chernyavsky, 2011), which allows the $\delta^{34}S$ of sulfide that diffuses upwards to the sediment surface to be determined by the ratio (Eq. (5)):

$$J(^{32}S)/J(^{34}S) = \frac{\partial[H_2{}^{32}S]}{\partial z} \Big/ \frac{\partial[H_2{}^{34}S]}{\partial z} \quad (5)$$

z is depth below the seafloor (Jørgensen, 1979; Jørgensen et al., 2004). Therefore, the $\delta^{34}S$ of porewater sulfide near the sediment surface can be derived from two end-members mixing (Eq. (6)):

$$Rate_{sum}\ F^{3X}S = Rate_{in-situSR}\ F^{3X}S_{in-situSR} + J_{diffusion}\ F^{3X}S_{diffusion} \quad (6)$$

where the $Rate_{sum}$ is the sum of $Rate_{in\text{-}situ\ SR}$ and $J_{diffusion}$, and the *F* represents fractional isotopic abundances of ^{32}S or ^{34}S (i.e., 3X = 32 or 34). $Rate_{sum}$ represents the gross rate of sulfide accumulation in the upper 5 cm of sediment, which is balanced by sulfide loss at steady state, resulting in H_2S concentrations below detection near the sediment surface. Since both oxidation of sulfide and precipitation of iron sulfide are considered to yield a negligible sulfur isotope fractionation (e.g., <5‰; Fry et al., 1986; Wilkin and Barnes, 1996; Böttcher et al., 1998b), sulfide loss is assumed to have no isotope effect, negating the need for a loss term in Eq. (6). The sensitivity of the model was tested by varying the depth ranges that SRR was intergraded (e.g., 0–3 or 0–10 cm) or, alternatively, by altering the magnitude of sulfur isotope fractionation (e.g., 60% or 66‰). Having a depth-integrated SRR beyond 10 cmbsf has negligible influence on the simulated outcome because SRR follows power decay function, decreasing rapidly with depth (Jørgensen, 1978; Beulig et al., 2018). Analogous calculations were performed for published data from four additional cores ($M1_{spring}$, $M1_{fall}$, M5 and M24) from Aarhus Bay, Baltic Sea (Brunner et al., 2016; Pellerin et al., 2018; Beulig et al., 2019).

3. RESULTS

3.1. Porewater geochemistry

Sites BB08, BB06 and BB07 feature three different types of pore-fluid profiles (Fig. 2b). At site BB08, sulfate concentrations steeply decrease with depth and sulfate is entirely consumed by 20 cmbsf. By contrast, although sulfate concentrations at sites BB06 and BB07 decrease slightly downcore, sulfate remains available throughout, reaching respective minima of 5.3 and 11.6 mM. Core BB08a and core 374190 show similar sulfate concentration profiles, with steep sulfate and methane gradients that define the sulfate–methane transition (SMT) at 18 cmbsf (Fig. 3a). Sulfate concentration near the sediment surface of core BB08d is 14.7 mM, which is slightly higher than that in cores BB08a and 374190. Gas escape structures such as pockmarks and acoustic plumes as an indication of rising gas bubbles in the water column were not observed in the Bornholm Basin, including site BB08 where the upper front of free methane gas bubbles was only ~60 cmbsf (Hilligsøe et al., 2018). Methane concentrations are below detection limit at sites BB06 and BB07. At sites BB08 and BB06, porewater sulfide concentrations increase linearly beneath the sediment surface, reaching respective maxima of 5.2 and 2.0 mM (Figs. 3b, 4b). Dissolved ferrous iron concentrations are low at sites BB08 and BB06, averaging 1.8 μM (Figs. 3b, 4b). At site BB07 no aqueous sulfide was detected, allowing accumulation of dissolved ferrous iron, which increases with depth to a maximum of 235 μM (Fig. 5a). Published porewater sulfate and methane profiles from sites BB01–BB05 are shown in Fig. 2b for comparison (Beulig et al., 2018; Liu et al., 2020a).

3.2. Solid-phase sediment geochemistry

Solid-phase sediment geochemistry was determined at sites BB08 and BB07. At site BB08, the CRS content increases with depth in the uppermost 5 cm, ranging from 12.8 to 77.2 umol g^{-1}, while ZVS contents are more or less invariant throughout the core (6.2 ± 1.6 umol g^{-1}, 1σ;

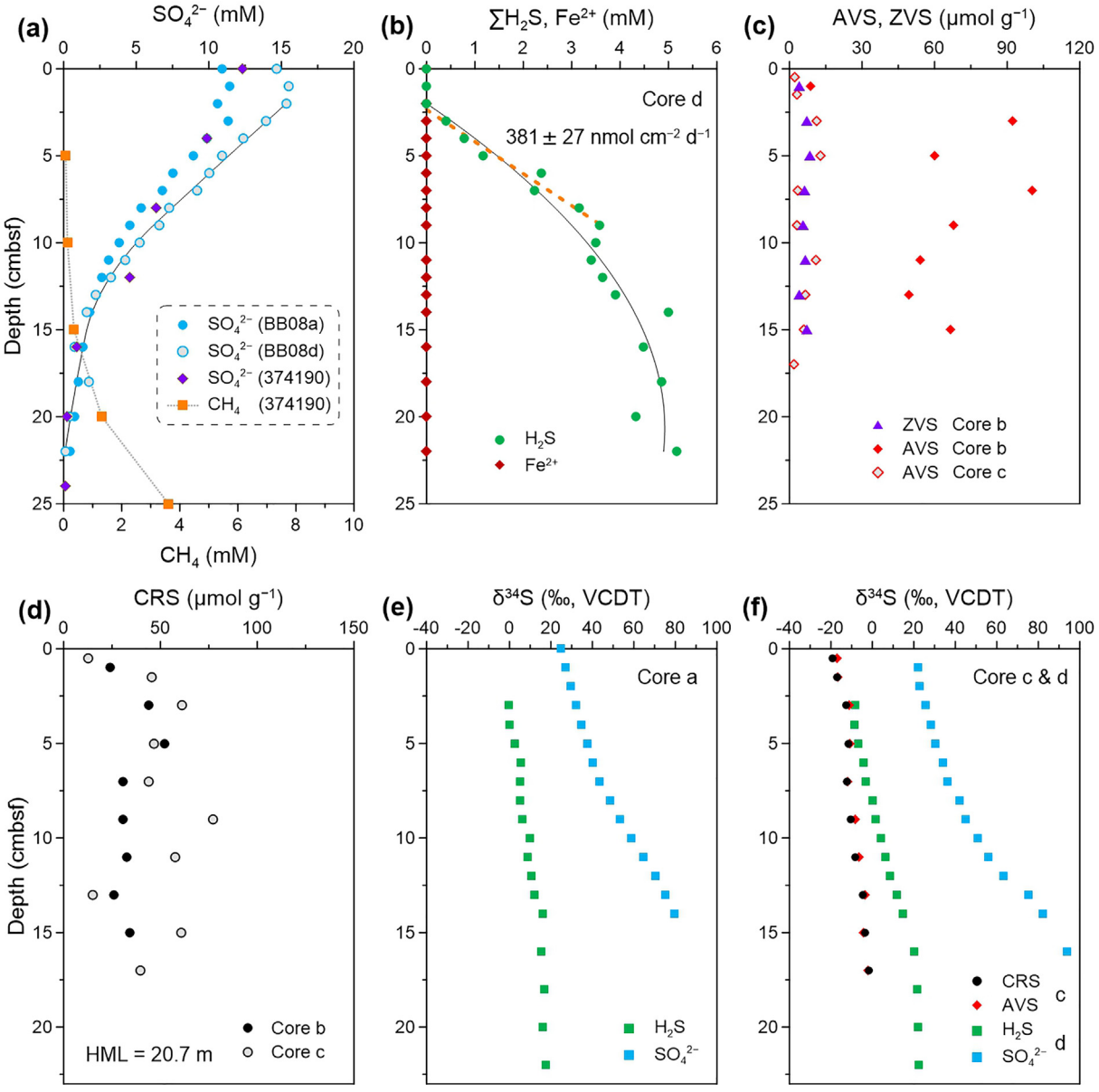

Fig. 3. Geochemical depth profiles from site BB08. Owing to the range of planned geochemical analysis, the site was cored four times, resulting in cores BB08a–d. (a) Porewater sulfate (cores BB08a, BB08d and 374190) and methane (core 374190) concentration. The solid black line represents the model fit to the sulfate concentration data obtained from core BB08d. Core 374190 was taken in 2009 at the same location as BB08 and is documented in Hilligsøe et al. (2018). (b) Porewater sulfide and ferrous iron concentration from core BB08d. The model fit to the sulfide data is illustrated as a solid black line, while the dashed orange line depicts a linear regression used to calculate the upward sulfide flux (381 ± 27 nmol cm^{-2} d^{-1}). (c) Acid volatile sulfur (AVS; cores BB08b–c) and zero-valent sulfur (ZVS; core BB08b) abundance. (d) Chromium reducible sulfur (CRS) abundance from cores BB08b (black) and BB08c (grey). (e–f) Sulfur isotopic composition of CRS (black circles), AVS (red diamonds), porewater sulfide (green squares) and sulfate (blue squares) from cores BB08a, BB08c and BB08d.

Fig. 3c–d). Surprisingly, the AVS contents within core BB08b (analyzed at Aarhus University one year after the cruise) are one order of magnitude higher than those in core BB08c (analyzed at MIT three years after the cruise). Although both cores were frozen at −20 °C until analysis, it appears that Fe monosulfides are sensitive to oxidation during storage and shipment (Rickard and Morse, 2005). Thus, we recommend freezing samples for AVS analysis at −20 °C under anoxic conditions and performing the extraction within one year of sampling, though abiotic oxidation of sulfides is considered to yield a negligible sulfur isotope fractionation (Fry et al., 1986; Balci et al., 2007; Zerkle et al., 2009).

At site BB07, the CRS contents range from 1.3 to 15.8 umol g^{-1} with isolated excursions to higher CRS contents encroaching on 117.1 umol g^{-1} at 7, 19 and 73 cmbsf (Fig. 5c). The AVS and ZVS contents display similar patterns at site BB07 and are mostly lower than 7.5 umol g^{-1}

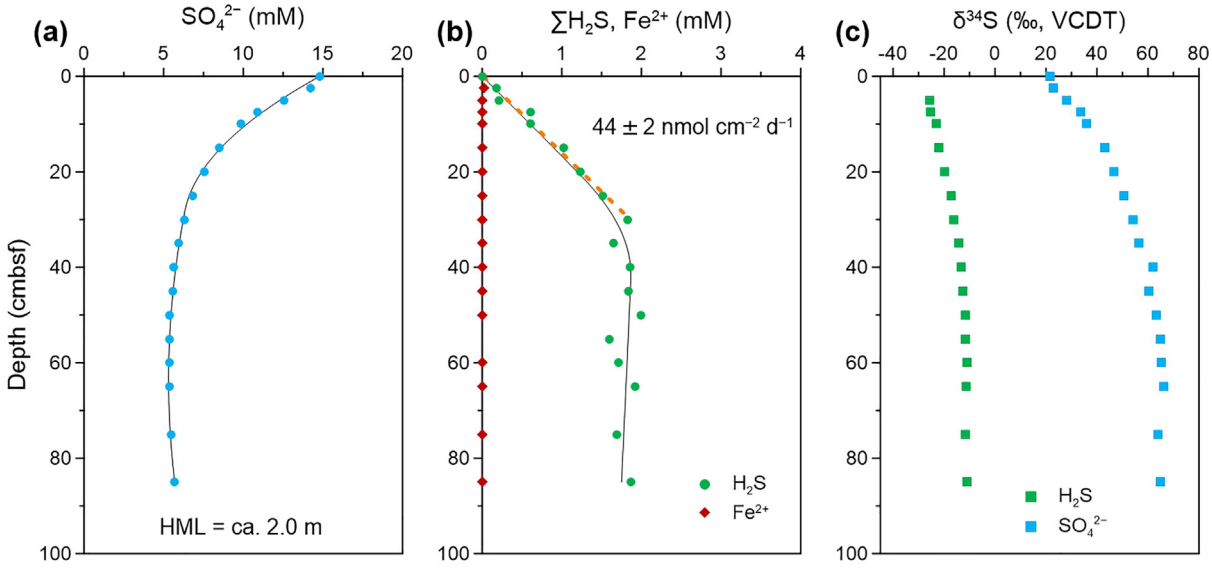

Fig. 4. Geochemical depth profiles from site BB06. (a) Porewater sulfate concentration (blue circles) and its model fit (solid black line). (b) Porewater sulfide (green circles) and ferrous iron (red diamonds) concentration. Here, the solid black line represents the model fit to the sulfide data, while the dashed orange line represents a linear regression used to calculate the upward sulfide flux (44 ± 2 nmol cm^{-2} d^{-1}). (c) Sulfur isotopic composition of porewater sulfate (blue squares) and sulfide (green squares).

with peaks at 19, 35 and 73 cmbsf (Fig. 5b). The HML comprises only the upper ~10 cm of site BB07, while the peaks of reduced sulfur species at 70–80 cmbsf potentially capture the transition to the brackish Yoldia Sea (Figs. 2a, 5b–c).

3.3. Sulfur and oxygen isotopes

The $\delta^{34}S$ of porewater sulfate increases downcore from 21‰ at the sediment–water interface to 93.8‰ and 66.1‰ at sites BB08 and BB06, respectively (Figs. 3e–f, 4c). Similarly, the $\delta^{34}S$ of porewater sulfide increases downcore from −0.3‰ to 17.5‰ in core BB08a, −8.4‰ to 22.2‰ in core BB08d, and −26.6‰ to −11.0‰ in core BB06 (Figs. 3e–f, 4c). The $\delta^{34}S$ values of CRS and AVS are largely similar in core BB08c, increasing from −19.3‰ to −1.7‰ with depth (Fig. 3f). The $\Delta^{33}S$ of CRS, however, shows a greater range of values (0.07–0.16‰) than $\Delta^{33}S$ of AVS (0.10–0.15‰) in core BB08c (Fig. 6). The $\delta^{34}S$ of CRS increases slightly downcore from −36.4‰ to −11.3‰ at site BB07 (Fig. 5d). The average $\delta^{34}S$ of CRS is −18.9‰ (±6.4‰,

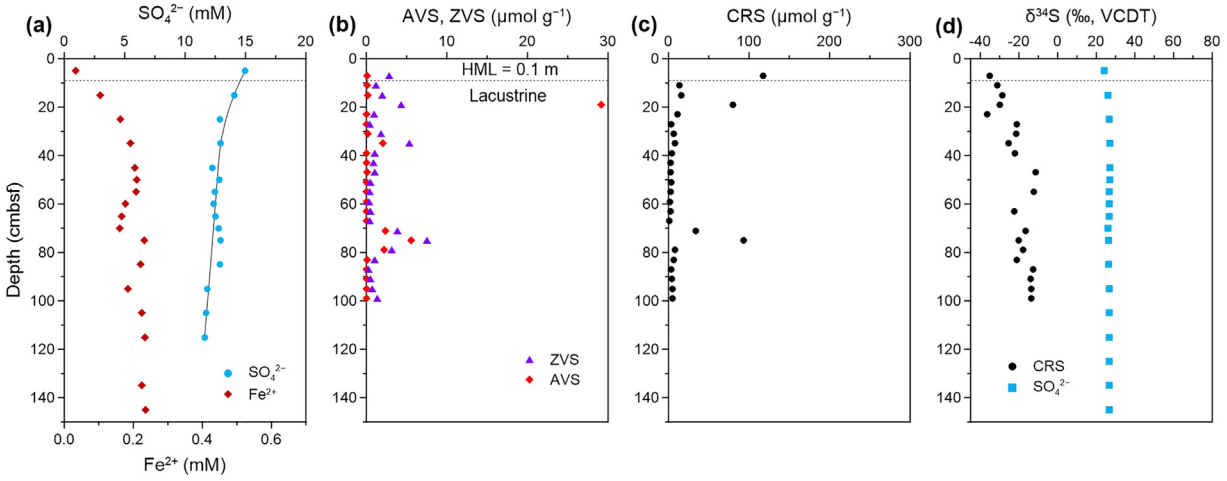

Fig. 5. Geochemical depth profiles from site BB07. (a) Porewater sulfate (blue circles) and ferrous iron (red diamonds) concentration. The black solid line depicts the model fit to the sulfate data. (b) Acid volatile sulfur (AVS; red diamonds), zero-valent sulfur (ZVS; purple triangles) and (c) chromium reducible sulfur (CRS; black circles) abundance. (d) Sulfur isotopic composition of CRS (black circles) and porewater sulfate (blue squares). The horizontal dashed lines represent the marine–lacustrine transition.

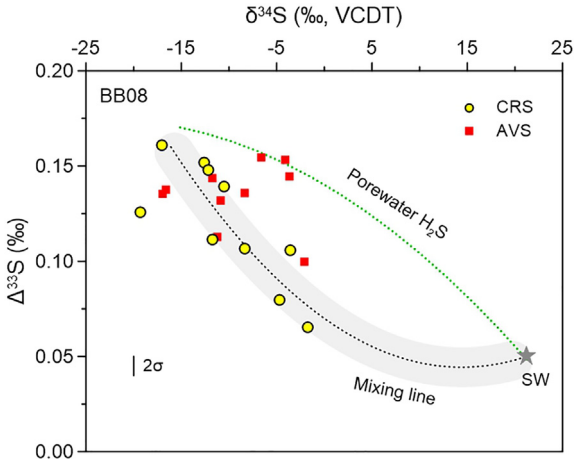

Fig. 6. Multiple sulfur isotope systematics of chromium reducible sulfur (CRS, yellow-filled circles) and acid volatile sulfur (AVS, red squares) extracted from site BB08. The green and black dotted curves represent the evolution of porewater sulfide (cf. Masterson, 2016) and the mixing line between early- and late-formed pyrite, respectively (cf. Liu et al., 2020b). SW abbreviates seawater sulfate. The 2-sigma uncertainty associated with the $\Delta^{33}S$ data is illustrated in the lower left.

1σ) at 20–100 cmbsf, which is consistent with $\delta^{34}S$ of CRS reported from the lacustrine clays within the Arkona Basin (ca. −20‰; Holmkvist et al., 2014).

The $\delta^{18}O$ of porewater sulfate increases with depth at all sites, ranging from 7.5‰ to 23.5‰ (Fig. 7). The slope of the apparent linear phase (SALP) of the cross plot between $\delta^{18}O$ and $\delta^{34}S$ is 0.21–0.23 at site BB08 but exceeds 0.41 at sites BB01–BB06. The $\delta^{18}O$ value of porewater sulfate increases from 12.0‰ to 15.5‰ downcore at site BB07 although the $\delta^{34}S$ value of porewater sulfate remains more or less constant at 26.5 ± 0.7‰ (1σ; Figs. 5d, 7c).

3.4. Sulfide flux and modeled rates of sulfide production and sulfate reduction

The estimated ascending diffusive sulfide flux shows a strong positive correlation with the thickness of the HML for the eight sites across the Bornholm Basin (exponential fit, $R^2 = 0.99$; Fig. 8a). For example, at site BB08, the upward sulfide flux is estimated at 381 ± 27 nmol cm^{-2} d^{-1} (1σ) where the HML thickness is 20.7 m, whereas, at site BB06, the upward sulfide flux is 44 ± 2 nmol cm^{-2} d^{-1} (1σ) where the HML thickness is ca. 2.0 m (Tables 1 and 2; Fig. 2c). The depth-integrated net sulfide production rate and net SRR are also positively correlated with the HML thickness and both are consistently higher than the upward sulfide flux (Table 2; Fig. 2c). The upward sulfide flux agrees with 90% (±8%, 1σ) of the integrated net sulfide production rate, suggesting that most, if not all, of the sulfide produced in the HML diffuses upward. Furthermore, the ascending sulfide flux displays a negative correlation with the $\delta^{34}S$ difference between porewater sulfate and sulfide (i.e., $\Delta^{34}S_{SO4\text{-}H2S}$) at 3 cmbsf (logarithmic fit, $R^2 = 0.92$), whereas less negative CRS $\delta^{34}S$ values at 3 cmbsf are associated with elevated sulfide fluxes (logarithmic fit, $R^2 = 0.84$; Fig. 8b–c). Since the $\delta^{34}S$ of porewater sulfate is less variable at 3 cmbsf (ca. 23‰), changes in $\Delta^{34}S_{SO4\text{-}H2S}$ at 3 cmbsf are largely due to changes in the $\delta^{34}S$ of porewater sulfide. Thus, the sulfate flux is not included here. Again, we selected 3 cmbsf because this is the shallowest depth where sulfide $\delta^{34}S$ data are typically available throughout the Bornholm Basin. These results are compared to those reported in the literature (Aharon and Fu, 2003; Strauss et al., 2012; Formolo and Lyons, 2013; Brunner et al., 2016; Hardisty et al., 2018; Pellerin et al., 2018; Liu et al., 2020a) as illustrated in Fig. 8.

4. DISCUSSION

4.1. The thickness of the Holocene Mud Layer modulates sulfate reduction and sulfide production

Porewater sulfate concentrations, and hence the shape of the downcore porewater sulfate profiles, within the Bornholm Basin are strongly correlated with the thickness of the HML (Fig. 2a–b). Using a dynamic reaction-transport model, Mogollón et al. (2012) analyzed the temporal evolution of porewater sulfate concentration profiles in the Arkona Basin in the wake of the marine transgression,

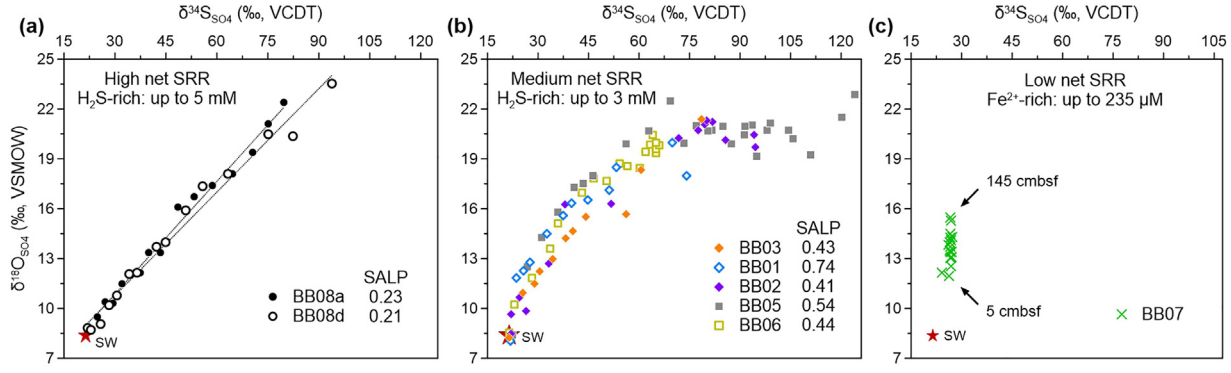

Fig. 7. The sulfur and oxygen isotope systematics of porewater sulfate isolated from various sites within the Bornholm Basin. Data are grouped according to the prevailing net sulfate reduction rate (SRR), with data in panel (a) derived from sulfide-replete site BB08 with a high SRR, those in panel (b) compiled from sites BB01–03, 05–06 with intermediate SRRs and those in panel (c) from iron-rich site BB07 with a low net SRR. Red stars denote the isotopic composition of seawater sulfate (SW). SALP abbreviates the slope of the apparent linear phase.

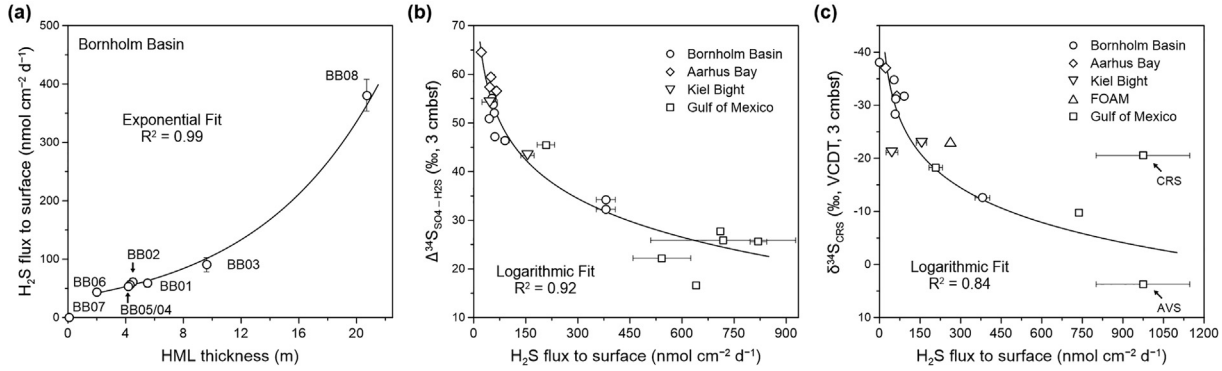

Fig. 8. The relationships between: (a) the thickness of the Holocene Mud Layer (HML) and the ascending sulfide flux, (b) the ascending sulfide flux and the isotopic difference between porewater sulfate and sulfide ($\Delta^{34}S_{SO4\text{-}H2S}$), and (c) the ascending sulfide flux and the isotopic composition of chromium reducible sulfur ($\delta^{34}S_{CRS}$) at 3 cmbsf. The curves represent exponential (a) or logarithmic (b, c) fits to the data and have been augmented with published data (b, c) from Aarhus Bay, Kiel Bight, the Gulf of Mexico and the Friends of Anoxic Mud site (FOAM; Aharon and Fu, 2003; Strauss et al., 2012; Formolo and Lyons, 2013; Brunner et al., 2016; Hardisty et al., 2018; Pellerin et al., 2018). Note that, in addition to sulfide diffusion from the depth, the $\delta^{34}S$ of pyrite near the sediment surface can also be influenced by externally-sourced pyrite (e.g., Liu et al., 2020b), sedimentary remobilization, and bioturbation (e.g., Fike et al., 2015). For example, the data points labeled AVS and CRS are from the Gulf of Mexico, obtained from a site where the $\delta^{34}S$ of H_2S more closely approximates that of AVS rather than CRS (Formolo and Lyons, 2013).

which led to the deposition of the organic-rich HML. Initially, during the early Holocene period, the marine incursion led to a salinity increase and increased sulfate diffusion into the pre-existing lacustrine clays, yet their organic-poor nature served to limit sulfate reduction (Holmkvist et al., 2014). As the HML thickened, however, the subsurface porewater sulfate concentrations slowly began to drop, a situation which we observe at site BB07 (Figs. 2b, 5a). Progressively, as the HML thickened further, a sulfate minimum developed (e.g., site BB06) prior to the complete consumption of sulfate within the marine mud (e.g., site BB05; Fig. 2b). The sulfate minimum induced upward diffusion of sulfate from the underlying lacustrine clay (Holmkvist et al., 2014), fostering the development of a methanogenic zone enveloped between two sulfate-bearing zones, as seen at site BB02 with an upper SMT at 0.7 mbsf (Fig. 2b). Ultimately, however, the deep porewater sulfate was depleted and a "normal" SMT developed.

One of the most striking characteristics of the Bornholm sedimentary succession is the negative relationship between the thickness of the HML and the depth of the SMT (Table 1; Fig. 2b). Using sediments from Aarhus Bay, Flury et al. (2016) demonstrated that the rates of methanogenesis and, thus, the upward diffusive flux of methane increase as the HML thickens. This increase in methane flux triggers a shallowing of the SMT, which subsequently exposes more organic-replete sediments in the HML to methanogenesis, forming feedback that further enhances methane production. Such positive feedback between methanogenesis and the depth of the SMT is also seen

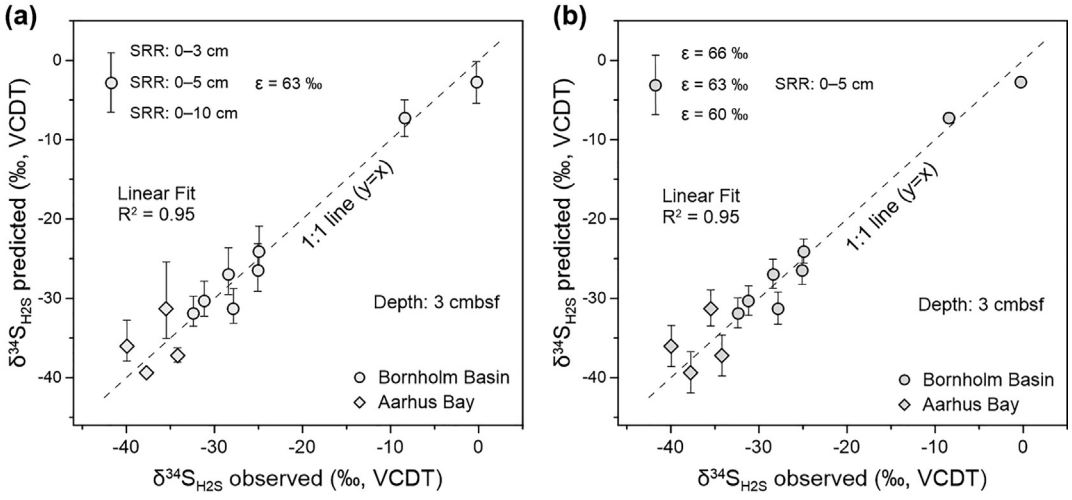

Fig. 9. Comparison between the measured (observed) and modeled (predicted) isotopic composition of aqueous sulfide ($\delta^{34}S_{H2S}$) at 3 cmbsf. The vertical error bars depict the outcome of different sensitivity experiments that explore the influence of (a) different integration depths for the calculation of the integrated SRR (0–3, 0–5, or 0–10 cm) or (b) the magnitude of sulfur isotope fractionation ($\varepsilon = 60$, 63 or 66‰). Data generated herein (circles) are augmented with data from the Aarhus Bay (diamonds; Brunner et al., 2016; Pellerin et al., 2018).

Table 2
Site-specific depth-integrated rates of sulfate reduction (SRR) and sulfide production combined with the resultant ascending sulfide flux and its isotopic composition ($\delta^{34}S$). Gross SRR are determined experimentally, while Net SRR and Net H_2S production rates are modeled from porewater gradients. Like the majority of the modeled data (b–c), experimentally determined sulfate reduction rates (a) are integrated throughout the sampled depth interval within the Holocene Mud Layer (HML; Beulig et al., 2018). Simulations pertaining to site BB07, however, integrate throughout the HML and into the deeper lacustrine clays (b–c). The fraction of sulfide derived from ascending flux and *in-situ* production in the upper 5 cm is shown in columns h–i. Here, $Rate_{sum}$ is the sum of $J_{diffusion}$ and $Rate_{in\text{-}situ\ SR}$ (see Section 2.6). N/A and n.d. abbreviate not applicable and not determined, respectively. Data in columns c and d are illustrated in Fig. 2.

Site	**a.** Gross SRR	**b.** Net SRR	**c.** Net H_2S production	**d.** Ascending H_2S flux	**e.** Net H_2S production (% of b)	**f.** Ascending H_2S flux (% of c)	**g.** $\delta^{34}S$ of ascending H_2S (‰, VCDT)	**h.** Ascending H_2S flux (% of $Rate_{sum}$)	**i.** *In-situ* H_2S production (% of $Rate_{sum}$)
	(nmol cm^{-2} d^{-1})								
BB08a	n.d.	476	n.d.	381	n.d.	n.d.	+6.3	81	19
BB08d	n.d.	457	408	381	89	93	+0.7	81	19
BB03	273	221	95	91	43	95	−7.9	50	50
BB01	276	238	80	59	33	73	−6.5	39	61
BB02	275	228	65	61	28	94	−6.1	40	60
BB05	309	166	59	53	35	91	−17.9	37	63
BB06	n.d.	227	46	44	20	96	−13.0	32	68
BB07	n.d.	35	0	0	0	N/A	N/A	0	100

within the Bornholm Basin (Hilligsøe et al., 2018) and the Black Sea (Henkel et al., 2012). As expected, the HML thickness strongly influences the depth-integrated rate of net sulfate reduction (Table 2). For example, the highest net SRRs (457–476 nmol cm^{-2} d^{-1}) are found at site BB08 where the SMT is very shallow, at 0.2 mbsf (Fig. 3a). This is because sulfate is completely consumed in the upper 20 cm where the SRR is the highest (Beulig et al., 2018). In contrast, the net SRR is only 35 nmol cm^{-2} d^{-1} at site BB07 with a very low sedimentation rate (1 cm ka^{-1}). Here, the HML is too thin for complete sulfate depletion and the SRR is essentially curtailed within the underlying organic-lean lacustrine clays by the lack of readily metabolizable carbon (Fig. 5a).

We note that ^{35}S-determined gross rates of sulfate reduction exceed the modeled net rates not only in the Bornholm Basin (Table 2) but also in Aarhus Bay, Limfjorden, the Black Sea and the eastern South Atlantic off Namibia (Fossing et al., 2000; Jørgensen et al., 2001; Jørgensen and Parkes, 2010; Dale et al., 2019). In reality, diffusion-reaction models (e.g., PROFILE) based solely on sulfate concentration gradients are unable to capture the elevated SRRs at the top of the zone of sulfate reduction if they do not account for elevated sulfate influx by bioirrigation, sulfide re-oxidation and the steep drop in reactivity of organic matter with sediment depth (Dale et al., 2019; Jørgensen et al., 2019a). These shortcomings are accentuated when oxygen availability is considered: in the hypoxic Bornholm Basin where bioirrigation and sulfide oxidation by oxygen are limited, gross rates of sulfate reduction are less than twice those of the net rates (Table 2), while the same discrepancy spans 1–2 orders of magnitude in sediments deposited beneath well-oxygenated water columns such as in Aarhus Bay and Limfjorden (Jørgensen and Parkes, 2010; Dale et al., 2019). These observations, therefore, strongly implicate bioirrigation and sulfide oxidation as drivers of the large discrepancies between the two approaches for determining SRR and demonstrate the need for more comprehensive modeling in these settings (e.g., Dale et al., 2019).

Sulfide availability within marine sediments is dictated by its sources and sinks. In general, sulfide is produced through OSR and sulfate reduction coupled to AOM. Drawing on data from the Baltic Sea, Jørgensen et al. (2019a) proposed that the majority of methane produced during methanogenesis permeates the SMT, fueling sulfate reduction rather than residing at depth. As the stoichiometry of sulfate-driven AOM is 1:1 (methane:sulfide, e.g., Martens and Berner, 1977; Niewöhner et al., 1998; Knittel and Boetius, 2009), the total sulfide production rate can be roughly considered as the sum of the rates of OSR and methanogenesis. Accepting that organic matter degradation within an anoxic sediment pile proceeds by OSR and/or methanogenesis, the total sulfide production rate is approximately equivalent to the total anaerobic carbon oxidation rate (COR) normalized for stoichiometric differences (Burdige, 2006). With highly depth-resolved analyses of geochemistry and microbial activities in the Bornholm Basin, Beulig et al. (2018) demonstrated that the COR has a power-law dependence on sediment age (in year BP): $COR = 1640 \times age^{-1.21}$ (nmol C cm^{-3} d^{-1}). Further, using a reaction-transport model, Dale et al. (2019) predicted an increase in COR across a transect of Aarhus Bay driven by an increase in the sediment accumulation rate. Therefore, the depth-integrated sulfide production rates are positively correlated with the thickness of the HML in the Bornholm Basin, as sulfide production is negligible in the organic-lean lacustrine clays (Fig. 2).

The major sinks for the subsurface sulfide pool in the Bornholm Basin include Fe-driven sulfide oxidation, precipitation of Fe-sulfide minerals and possibly organic matter sulfurization (e.g., Jørgensen and Kasten, 2006; Raven et al., 2016; Jørgensen et al., 2019b). Findlay et al. (2020) found that Fe-driven sulfide oxidation could no longer be quantified below 10 cmbsf in Aarhus Bay. In the Bornholm Basin, much of the pyrite is rapidly formed near the sediment–water interface and subsequent pyrite accumulation occurs slowly with depth (Liu et al., 2020a). These results suggest that subsurface sulfide oxidation and pyrite formation within the HML are strongly controlled by the amount

and reactivity of Fe-oxides, allowing aqueous sulfide to accumulate in pore fluids at depth. Consequently, the greater the thickness of the HML, the higher the depth-integrated net sulfide production rates and thus the resultant sulfide fluxes towards the surface (Figs. 2c, 8a). Among the study sites, 90% (±8%, 1σ) of the aqueous sulfide diffuses upward toward the sediment surface (Table 2; Fig. 2c), while the remaining 10% diffuses down toward the sulfidization front where it reacts with Fe-oxides and Fe^{2+} to form Fe-sulfide minerals. This contrasts with observations from the Black Sea where more than 50% of the sulfide produced in sediments diffuses downward toward the sulfidization front (Jørgensen et al., 2004). This difference between these two basins is caused by the greater proximity of the sulfidization fronts in the Black Sea to the locus of peak sulfide production at the depth of the SMT (about 2 mbsf in the Black Sea; Jørgensen et al., 2004; Neretin et al., 2004; Holmkvist et al., 2014; Liu et al., 2020a). The sulfidization of the deep Fe(III)-rich clays, however, does not continue indefinitely. For instance, at site BB03, the H_2S-Fe^{2+} interface has migrated upwards and currently resides at 5–6 mbsf within the HML, whereas the paleo-sulfidization front was located near the fresh–brackish water transition at ca. 10 mbsf (Andrén et al., 2015; Egger et al., 2017; Liu et al., 2021). The high sedimentation rate at site BB03 separates the depth of sulfate penetration, and thus the maximum depth of H_2S formation, from the lacustrine clays over time, which ultimately terminates the sulfidization of the deep Fe-oxide minerals (Liu et al., 2020a).

4.2. Isotopically "heavy" sulfides near the sediment surface due to high upward flux of sulfide

Microbial sulfate reduction preferentially consumes ^{32}S over ^{34}S, resulting in a sulfur isotope fractionation that may approach 70‰ (Wortmann et al., 2001; Brunner and Bernasconi, 2005; Sim et al., 2011a). This process, therefore, enriches porewater sulfate in ^{34}S that propagates to the subsequently-produced sulfide (Canfield, 2001; Turchyn et al., 2016; Pellerin et al., 2018). The magnitude of the sulfur isotope fractionation accompanying sulfate reduction is controlled by the cell-specific rate of sulfate reduction, which in turn largely reflects the availability of electron donors (e.g., H_2, acetate, methane) in marine sediments (Jin and Bethke, 2009; Sim et al., 2011a; Deusner et al., 2014; Jørgensen et al., 2019b). As the key parameter controlling the expression of sulfur isotope fractionation, the csSRR is generally found to be low (10^{-6}–10^{-1} fmol $cell^{-1}$ day^{-1}) in marine sediments owing to low electron donor availability (Hoehler and Jørgensen, 2013; Glombitza et al., 2019; Jørgensen et al., 2019b). *In vitro* approaches demonstrate a negative correlation between the csSRR and the magnitude of sulfur isotope fractionation, where sulfur isotope fractionation is muted (<40‰) when csSRRs exceed ~1 fmol $cell^{-1}$ day^{-1} (Sim et al., 2011a, 2011b; Leavitt et al., 2013). Both the SRR and the abundance of sulfate-reducing microorganisms are found to be at their highest near the sediment–water interface and decrease steeply with depth, maintaining low csSRRs (<0.1 fmol $cell^{-1}$ day^{-1}) throughout the sediment column within Aarhus Bay (Leloup et al., 2009; Holmkvist et al., 2011; Petro et al., 2019) and most likely within the Bornholm Basin (Beulig et al., 2018). Accordingly, the low csSRR, along with the nearly constant total organic carbon content (4.9 ± 0.7 wt %) among the study sites, suggest that the magnitude of the sulfur isotope fractionation is large and constant (ca. 63‰; see Section 2.6) in the Bornholm Basin, even in proximity to the sediment–water interface where both the reactivity of buried organic matter and the abundance of sulfate-reducing microorganisms are the highest.

Although the sulfur isotope fractionation remains large and the $\delta^{34}S$ of porewater sulfide increases in parallel to that of porewater sulfate (Figs. 3e–f, 4c), the magnitude of their downcore increase depends largely on the extent of sulfate depletion. At site BB08, for example, the $\delta^{34}S$ of H_2S in the SMT approaches +21‰ (Fig. 3e–f). The $\delta^{34}S$ of H_2S increases to −11.0‰ at site BB06 where sulfate concentrations only reach a minimum of 5.3 mM (Fig. 4c). At site BB07, however, the $\delta^{34}S$ of sulfate increases only by 3.1‰ throughout the core due to very weak activity of sulfate reduction in the lacustrine clays (Fig. 5d).

Importantly, the distribution of sulfur isotopes among various sulfur-bearing phases in the sediment is ultimately controlled by open system diffusion. The H_2S concentration decreases towards the sediment surface, indicating the diffusive H_2S flux upward. The downcore increase in H_2S concentration and its $\delta^{34}S$ fosters the relative enrichment of $H_2^{34}S$ with depth relative to $H_2^{32}S$, culminating in a steeper $H_2^{34}S$ gradient than its ^{32}S isotopologue (Jørgensen, 1979; Jørgensen et al., 2004). Accordingly, the diffusive H_2S flux carries a higher $\delta^{34}S$ value (e.g., +0.7‰ in core BB08d; Table 2), than that of the native porewater H_2S pool at 3 cmbsf (e.g., −8.4‰ in core BB08d; Fig. 3f). In simpler terms, the ascending diffusive H_2S flux serves as a vector of ^{34}S to the sediment surface. Similarly, the downward diffusing sulfate is enriched in ^{32}S relative to the ambient porewater sulfate pool, thereby reducing the effect of isotope fractionation associated with sulfate reduction in the subsurface sediment (Jørgensen, 1979; Goldhaber and Kaplan, 1980; Chanton et al., 1987). The net result is the formation of H_2S in the SMT with a $\delta^{34}S$ value close to that of seawater sulfate (+21‰; Jørgensen et al., 2004).

Deusner et al. (2014) demonstrated that the sulfur isotope fractionation associated with sulfate reduction coupled to AOM at gas seeps, where methane concentrations are high (e.g., >5 mM), is much smaller (i.e., 20–40‰) than that observed within an SMT located at greater depth within the sediment pile (>60‰). The sulfur isotope fractionation at site BB08 is therefore expected to be large (>60‰) since the methane concentrations are consistently low in the sulfate zone (0.07–1.32 mM; Fig. 3a). The isotopic difference between porewater sulfate and sulfide, however, is found to be smaller (34.2‰) at 3 cmbsf of site BB08 (Fig. 3f). This discrepancy is the result of mixing between the ^{34}S-enriched sulfide ascending from below (+0.7‰) and the ^{34}S-depleted sulfide produced *in-situ* (ca. −40‰).

Following the method described in Section 2.6, a simple mixing model was used to understand the $\delta^{34}S$ of H_2S in the

surface sediments of the Baltic Sea (Fig. 9). There is excellent agreement between the model output and the measured $\delta^{34}S$ of H_2S even with a range of sensitivity tests (Fig. 9). Moreover, the isotopic similarity among all reduced sulfur species at 3 cmbsf suggests that the $\delta^{34}S$ values of pyrite and Fe monosulfides are inherited from H_2S (Fig. 3f). Consequently, our results demonstrate that upward diffusion of isotopically "heavy" sulfide can, indeed, result in high $\delta^{34}S$ values seen in H_2S and thus pyrite near the sediment surface despite a large expected sulfur isotope fractionation at shallow depths. This conclusion is important because the sulfide flux determines the initial $\delta^{34}S$ of pyrite and a change in sulfide flux could cause a substantial change in the recorded $\delta^{34}S$ of pyrite, which is relevant on geological timescales. This potentially explains why the initial pyrite formed in proximity to the sediment–water interface at two adjacent sites (BB02 and BB05) varied at least 6‰ on sub-millennial timescales (Liu et al., 2020a).

To test the importance of the ascending sulfide flux on a larger spatial scale, we compiled concentration and isotope data from five marine settings (Aharon and Fu, 2003; Strauss et al., 2012; Formolo and Lyons, 2013; Brunner et al., 2016; Hardisty et al., 2018; Pellerin et al., 2018; Liu et al., 2020a). Focusing on data from 3 cmbsf, when the ascending H_2S flux strengthens, the associated $\Delta^{34}S_{SO4\text{-}H2S}$ values decrease and CRS-$\delta^{34}S$ increase (Fig. 8b–c). This means that $d[H_2S]/dz$ is positively correlated with the $\delta^{34}S$ of aqueous sulfide near the sediment surface. In the seep-influenced sediments from the Gulf of Mexico, the high sulfide fluxes are likely accompanied by elevated methane concentrations and thus the muted $\Delta^{34}S_{SO4\text{-}H2S}$ values may reflect a combination of depth-derived ^{34}S-adulterated sulfide and smaller magnitude isotope fractionation associated with sulfate-driven AOM (e.g., Deusner et al., 2014). Moreover, given the likelihood of porewater mixing induced by bubble ebullition or bioirrigation by chemosynthetic macrofauna, advective transport should also be considered at active seep sites (e.g., Fischer et al., 2012). In summary, it is necessary to take the effect of diffusion and/or advection into account to understand the sulfur isotope fractionation and sulfur isotopic signals of pyrite, barite and carbonate-associated sulfate, not only in methane seeps but also in a wider range of marine sediments.

The $\delta^{34}S$ of pyrite increased by 17.6‰ between 1 and 17 cmbsf at site BB08 (Fig. 3f). The ^{34}S-enriched pyrite in the subsurface sediments reflects the combined product of early- and late-formed pyrite, as indicated by its multiple sulfur isotope systematics. The measured $\delta^{34}S$ and $\Delta^{33}S$ of early-formed pyrite at 1.5 cmbsf are −17‰ and 0.16‰, respectively (Fig. 6), while their late-formed counterparts approximate those of seawater sulfate ($\delta^{34}S$ = 21‰, $\Delta^{33}S$ = 0.05‰) due to differential diffusion of ^{32}S, ^{33}S and ^{34}S (Jørgensen et al., 2004; Liu et al., 2020b). The $\delta^{34}S$ and $\Delta^{33}S$ systematics of pyrite extracted from site BB08 adorn the mixing line between these two pyrite pools (Fig. 6), where mixing results in curved trajectories and progressively lower $\Delta^{33}S$ values (0.07‰; Ono et al., 2006). Although the $\delta^{34}S$ of Fe monosulfides is highly similar to that of pyrite throughout the core (Fig. 3f), a different pattern in $\Delta^{33}S$ values is seen between the two sulfur species (Fig. 6). Some $\Delta^{33}S$ values of Fe monosulfides approach the higher $\Delta^{33}S$ values of porewater sulfide (up to 0.15‰), supporting the inference that active isotope exchange occurs between aqueous sulfide and the surface of Fe monosulfide minerals (Fossing and Jørgensen, 1990; Fossing et al., 1992; Liu et al., 2020a).

The near-surface-pyrite contents vary across the basin and correlate with the sedimentation rate. For example, a lower pyrite content of 13 μmol S g^{-1} was determined at site BB08 with a high sedimentation rate of 244 cm ka^{-1} (Fig. 3d), whereas sites BB01–BB05 have higher pyrite contents of 27–62 μmol S g^{-1} at the sediment surface (Liu et al., 2020a, 2021) but lower sedimentation rates of 49–113 cm ka^{-1} (Table 1). The low pyrite content at site BB08 can be partly explained by dilution with clastic material. Additionally, higher sedimentation rates serve to lower the contact time between the sulfidic porewaters and reactive Fe-oxide minerals, promoting the burial and preservation of Fe-oxides but also limiting pyrite formation (Riedinger et al., 2005; Fu et al., 2008; März et al., 2008). As a result, decreased pyrite precipitation close to the sediment–water interface will promote an increase in pyrite-$\delta^{34}S$ with depth (Liu et al., 2021) as seen at site BB08, whereas rapid pyrite formation at the sediment surface and low availability of reactive Fe at depth allow the isotopic signal of early-formed ^{32}S-enriched pyrite ($\delta^{34}S \approx -30$‰) to be preserved in deeper sediments at the low-sedimentation sites BB01/02/05 (Liu et al., 2020a). Collectively, we conclude that, provided that reactive iron is available at depth, the upward diffusion of isotopically "heavy" sulfide and the initial pyrite content regulate the initial $\delta^{34}S$ of pyrite near the sediment surface and the extent of the increase in $\delta^{34}S$ with depth, respectively, both controlling pyrite-$\delta^{34}S$ values in subsurface sediments.

4.3. Sulfur and oxygen isotopic composition of porewater sulfate

The coupled sulfur and oxygen isotopic composition of porewater sulfate have been widely used to explore sulfate-reducing metabolisms in marine sediments (Böttcher et al., 1998a; Aharon and Fu, 2000, 2003; Turchyn et al., 2006; Antler et al., 2015). Previous studies have shown that, in a given porewater profile, the slope of the tangent on the $\delta^{18}O_{SO4}$ *versus* $\delta^{34}S_{SO4}$ crossplot (i.e., SALP) is related to the net SRR and that higher rates lower the SALP (Böttcher et al., 1998a, 1999; Brunner et al., 2005, 2012; Antler et al., 2013). Antler et al. (2013) demonstrated that the rate of intracellular sulfite oxidation is the key parameter controlling the relative evolution of sulfur and oxygen isotopes in porewater sulfate during sulfate reduction. The SALP is also affected by extracellular sulfur cycling when reduced sulfur species are re-oxidized (e.g., Böttcher and Thamdrup, 2001). The SALP, however, is relatively unaffected by changes in transport and non-steady state dynamics (Fotherby et al., 2021). In sedimentary environments where net SRR is high, such as cold seeps, estuaries and mangroves, the degree of sulfur re-cycling is minimal and the $\delta^{18}O$ of porewater sulfate increases less steeply relative to its $\delta^{34}S$ value (i.e., SALP < ~0.4; Aharon and Fu, 2000,

2003; Antler et al., 2014, 2015; Crémière et al., 2017). In contrast, in environments where net SRR is low, such as (hemi) pelagic sediments and some shelf settings with deep or non-existent SMTs, sulfur re-cycling is much more extensive and the $\delta^{18}O$ of porewater sulfate increases more steeply relative to the $\delta^{34}S$ (i.e., SALP > ~0.4; Turchyn et al., 2006; Aller et al., 2010; Riedinger et al., 2010; Mills et al., 2016).

Sediments in the Bornholm Basin display a large range of SALP, reflecting the large range of net SRR across the basin (Fig. 7). For example, very low SALP values (0.21–0.23) are seen at the sulfide-rich site BB08 where net SRRs are the highest (457–476 nmol cm^{-2} d^{-1}; Fig. 7a). This reflects the fact that sulfate reduction at site BB08 is less electron-donor limited due to the highly reactive organic matter in the surface sediment and a large flux of methane to the SMT (Fig. 2b). High OSR activity and sulfate-driven-AOM in the shallow SMT lower the reversibility along the enzymatic pathway of sulfate reduction and hence limits sulfite re-oxidation that causes the observed low SALP (Antler et al., 2015; Feng et al., 2016; Antler and Pellerin, 2018). As expected, sites with intermediate net SRRs (216 ± 29 nmol cm^{-2} d^{-1}, 1σ) are associated with higher SALP values (0.41–0.74; Fig. 7b). While many of these sites (i.e., BB03, BB01 and BB02) are methane-rich at and below the SMT (Liu et al., 2020a, 2021), near-surface OSR has driven $\delta^{18}O_{SO4}$ to equilibrium before sulfate-driven AOM at the deep-seated SMTs has been reached (Antler and Pellerin, 2018). Site BB07 represents an end-member with a low net SRR (35 nmol cm^{-2} d^{-1}). While the $\delta^{18}O_{SO4}$ increases downcore, the $\delta^{34}S_{SO4}$ remains constant (Fig. 7c). The organic-lean lacustrine clays are known to be highly iron(III)-rich (Böttcher and Lepland, 2000; Holmkvist et al., 2014; Liu et al., 2020a), allowing intensive oxidative sulfur re-cycling to occur. Thus, a large part of the sulfate that is reduced is ultimately re-oxidized. This cryptic sulfur cycle prevents aqueous sulfide and pyrite accumulation in the iron(III)-rich sediment but promotes the subsequent build-up of Fe^{2+} in porewater (Fig. 5).

Taken together, the interplay between iron, sulfur and methane is in stark contrast between the sulfide- and iron-rich sediments due to their depositional history and sediment properties. Since the type and reactivity of organic matter and availability of reactive iron modulate sulfide production and consumption (Berner, 1984; Middelburg, 1991; Kasten et al., 1998; Fu et al., 2008; Roberts, 2015; Shawar et al., 2018), the ultimate controlling factor of isotopic signature of porewater sulfate is the availability of organic carbon *vs.* reactive iron. This results in a remarkable difference preserved within the coupled sulfur and oxygen isotope systematics of porewater sulfate between the two sedimentary systems (cf. Antler et al., 2019). Thus, the SALP provides a powerful tool to study the biogeochemical sulfur cycle because it is sensitive to changes in the net SRR *versus* the oxidation of reduced sulfur species (Antler and Pellerin, 2018).

5. CONCLUSIONS

Combining seismo-acoustic mapping with geochemical analyses of sediment cores demonstrates that the concentration and isotope systematics of porewater sulfate and sulfide within the upper ten meters of the Bornholm Basin sedimentary succession are influenced by the thickness of the organic-rich Holocene Mud Layer (HML), with a higher sedimentation rate fueling elevated total anaerobic carbon oxidation rates and thus higher SRR and sulfide production rates. Based on the modeled net sulfide production rate and the measured ascending sulfide flux, the majority of the sulfide produced at depth diffuses upward. Importantly, a thicker HML increases the ascending sulfide flux, serving as a spatially variable vector of relatively ^{34}S-enriched sulfide to the shallow porewater sulfide pool. Beyond the adulteration of the native shallow sulfide pool ($\delta^{34}S = -0.3‰$), this influx of ^{34}S-enriched sulfide is subsequently preserved in sedimentary pyrite. A simple mixing model and compilation of sulfur isotope data from other marine settings suggest that the upward diffusion of ^{34}S-enriched sulfide can be an important factor controlling the $\delta^{34}S$ value of pyrite formed in shallow marine organic-rich successions. The sulfur and oxygen isotope systematics of porewater sulfate are also related to the net SRR. Here, within high SRR regimes, the ^{18}O-enrichment in porewater sulfate is more muted when compared to the ^{34}S-enrichment while, in low SRR regimes, $\delta^{18}O_{SO4}$ values increase downcore while the associated $\delta^{34}S_{SO4}$ values remain effectively invariant. Taken together, it is clear that sedimentation rates and differential diffusion fluxes of the two sulfur isotopes in porewater sulfide and sulfate control the fate of sulfur on the basin-scale, exerting an important influence on the isotopic signature of sulfur-bearing species. This work highlights the importance of considering the local depositional environment and open system pore-fluid transport when interpreting $\delta^{34}S$ signals, especially in lithologically heterogenous successions.

Declaration of Competing Interest

The authors declare that they have no known competing financial interests or personal relationships that could have appeared to influence the work reported in this paper.

ACKNOWLEDGMENTS

We acknowledge the skipper and crew of the R/V *Aurora*, as well as colleagues at the Center for Geomicrobiology, for assistance during sampling. We recognize contributions and technical assistance from Susann Henkel, Ingrid Dohrmann, Ingrid Stimac, Jeanette Pedersen, Karina Bomholt Oest and Felix Beulig. We thank Virgil Pasquier and two anonymous reviewers for their helpful and constructive reviews of this paper. This work was supported by the Danish National Research Foundation (DNRF grant #104), the Danish Council for Independent Research (DFF – 7014-00196), the European Research Council (ERC Advanced Grant #294200), the Helmholtz Association (Alfred Wegener Institute Helmholtz Centre for Polar and Marine Research in Bremerhaven) and the Alfred P. Sloan Foundation via the Deep Carbon Observatory. JL acknowledges a NASA FINESST Fellowship (80NSSC21K1529). AP is supported by the Zuckerman STEM Leadership Program. GA acknowledges financial support from the Israel Science Foundation (2361/19). GI recognizes a MISTI award ("Decrypting Early Earth's Oxygenation") in addition to

continued support from Roger Summons under the auspices of the Simons Collaboration on the Origin of Life. AF is supported by a Marie-Curie European Fellowship (SedSulphOx, MSCA 746872). AVT acknowledges financial support from the National Environmental Research Council (NERC–NE/T006838/1). JL gratefully recognizes continued support from, and discussions with, Tina Treude and Jiasheng Wang.

APPENDIX A. SUPPLEMENTARY MATERIAL

Supplementary data to this article can be found online at https://doi.org/10.1016/j.gca.2021.08.018.

REFERENCES

Aharon P. and Fu B. (2000) Microbial sulfate reduction rates and sulfur and oxygen isotope fractionations at oil and gas seeps in deepwater Gulf of Mexico. *Geochim. Cosmochim. Acta* **64**, 233–246.

Aharon P. and Fu B. (2003) Sulfur and oxygen isotopes of coeval sulfate–sulfide in pore fluids of cold seep sediments with sharp redox gradients. *Chem. Geol.* **195**, 201–218.

Aller R. C., Madrid V., Chistoserdov A., Aller J. Y. and Heilbrun C. (2010) Unsteady diagenetic processes and sulfur biogeochemistry in tropical deltaic muds: Implications for oceanic isotope cycles and the sedimentary record. *Geochim. Cosmochim. Acta* **74**, 4671–4692.

Andrén E., Andrén T. and Sohlenius G. (2000) The Holocene history of the southwestern Baltic Sea as reflected in a sediment core from the Bornholm Basin. *Boreas* **29**, 233–250.

Andrén T., Jørgensen B. B., Cotterill C., Green S. and Expedition 347 Scientists (2015) Site M0065. In *Proceedings of the Integrated Ocean Drilling Program* (ed. T. Andrén). Integrated Ocean Drilling Program, College Station, Texas.

Antler G., Mills J. V., Hutchings A. M., Redeker K. R. and Turchyn A. V. (2019) The sedimentary carbon-sulfur-iron interplay – A lesson from east Anglian salt marsh sediments. *Front. Earth Sci.* **7** 140.

Antler G. and Pellerin A. (2018) A critical look at the combined use of sulfur and oxygen isotopes to study microbial metabolisms in methane-rich environments. *Front. Microbiol.* **9** 519.

Antler G., Turchyn A. V., Herut B., Davies A., Rennie V. C. F. and Sivan O. (2014) Sulfur and oxygen isotope tracing of sulfate driven anaerobic methane oxidation in estuarine sediments. *Estuar. Coast. Shelf Sci.* **142**, 4–11.

Antler G., Turchyn A. V., Herut B. and Sivan O. (2015) A unique isotopic fingerprint of sulfate-driven anaerobic oxidation of methane. *Geology* **43**, 619–622.

Antler G., Turchyn A. V., Rennie V., Herut B. and Sivan O. (2013) Coupled sulfur and oxygen isotope insight into bacterial sulfate reduction in the natural environment. *Geochim. Cosmochim. Acta* **118**, 98–117.

Balci N., Shanks W. C., Mayer B. and Mandernack K. W. (2007) Oxygen and sulfur isotope systematics of sulfate produced by bacterial and abiotic oxidation of pyrite. *Geochim. Cosmochim. Acta* **71**, 3796–3811.

Baune C. and Böttcher M. E. (2010) Experimental investigation of sulphur isotope partitioning during outgassing of hydrogen sulphide from diluted aqueous solutions and seawater. *Isotopes Environ. Health Stud.* **46**, 444–453.

Berg P., Risgaard-Petersen N. and Rysgaard S. (1998) Interpretation of measured concentration profiles in sediment pore water. *Limnol. Oceanogr.* **43**, 1500–1510.

Berner R. A. (1970) Sedimentary pyrite formation. *Am. J. Sci.* **268**, 1–23.

Berner R. A. (1984) Sedimentary pyrite formation: An update. *Geochim. Cosmochim. Acta* **48**, 605–615.

Beulig F., Røy H., Glombitza C. and Jørgensen B. B. (2018) Control on rate and pathway of anaerobic organic carbon degradation in the seabed. *P. Natl. Acad. Sci. USA* **115**, 367–372.

Beulig F., Røy H., McGlynn S. E. and Jørgensen B. B. (2019) Cryptic CH_4 cycling in the sulfate–methane transition of marine sediments apparently mediated by ANME-1 archaea. *ISME J.* **13**, 250–262.

Böttcher M. E., Bernasconi S. M. and Brumsack H. J. (1999) Carbon, sulfur, and oxygen isotope geochemistry of interstitial waters from the western Mediterranean. *Proc. ODP Sci. Res.* **161**, 413–421.

Böttcher M. E., Brumsack H. J. and De Lange G. J. (1998a) Sulfate reduction and related stable isotope (^{34}S, ^{18}O) variations in interstitial waters from the Eastern Mediterranean. *Proc. ODP Sci. Res.* **160**, 365–373.

Böttcher M. E. and Lepland A. (2000) Biogeochemistry of sulfur in a sediment core from the west-central Baltic Sea: Evidence from stable isotopes and pyrite textures. *J. Mar. Syst.* **25**, 299–312.

Böttcher M. E., Smock A. M. and Cypionka H. (1998b) Sulfur isotope fractionation during experimental precipitation of iron (II) and manganese(II) sulfide at room temperature. *Chem. Geol.* **146**, 127–134.

Böttcher M. E. and Thamdrup B. (2001) Anaerobic sulfide oxidation and stable isotope fractionation associated with bacterial sulfur disproportionation in the presence of MnO_2. *Geochim. Cosmochim. Acta* **65**, 1573–1581.

Bottrell S. H. and Newton R. J. (2006) Reconstruction of changes in global sulfur cycling from marine sulfate isotopes. *Earth-Sci. Rev.* **75**, 59–83.

Brunner B., Arnold G. L., Røy H., Müller I. A. and Jørgensen B. B. (2016) Off limits: Sulfate below the sulfate-methane transition. *Front. Earth Sci.* **4**, 75.

Brunner B. and Bernasconi S. M. (2005) A revised isotope fractionation model for dissimilatory sulfate reduction in sulfate reducing bacteria. *Geochim. Cosmochim. Acta* **69**, 4759–4771.

Brunner B., Bernasconi S. M., Kleikemper J. and Schroth M. H. (2005) A model for oxygen and sulfur isotope fractionation in sulfate during bacterial sulfate reduction processes. *Geochim. Cosmochim. Acta* **69**, 4773–4785.

Brunner B., Einsiedl F., Arnold G. L., Müller I., Templer S. and Bernasconi S. M. (2012) The reversibility of dissimilatory sulphate reduction and the cell-internal multi-step reduction of sulphite to sulphide: insights from the oxygen isotope composition of sulphate. *Isotopes Environ. Health Stud.* **48**, 33–54.

Burdige D. J. (2006) *Geochemistry of marine sediments*. Princeton University Press, Princeton, New Jersey.

Canfield D. and Thamdrup B. (1994) The production of ^{34}S-depleted sulfide during bacterial disproportionation of elemental sulfur. *Science* **266**, 1973–1975.

Canfield D. E. (2001) Biogeochemistry of Sulfur Isotopes. *Rev. Mineral Geochem.* **43**, 607–636.

Carstensen J., Andersen J. H., Gustafsson B. G. and Conley D. J. (2014) Deoxygenation of the Baltic Sea during the last century. *P. Natl. Acad. Sci. USA* **111**, 5628–5633.

Chanton J. P., Martens C. S. and Goldhaber M. B. (1987) Biogeochemical cycling in an organic-rich coastal marine basin. 8. A sulfur isotopic budget balanced by differential diffusion across the sediment-water interface. *Geochim. Cosmochim. Acta* **51**, 1201–1208.

Cline J. D. (1969) Spectrophotometric determination of hydrogen sulfide in natural waters. *Limnol. Oceanogr.* **14**, 454–458.

Crémière A., Strauss H., Sebilo M., Hong W.-L., Gros O., Schmidt S., Tocny J., Henry F., Gontharet S. and Laverman A. M. (2017) Sulfur diagenesis under rapid accumulation of organic-rich sediments in a marine mangrove from Guadeloupe (French West Indies). *Chem. Geol.* **454**, 67–79.

Dale A. W., Flury S., Fossing H., Regnier P., Røy H., Scholze C. and Jørgensen B. B. (2019) Kinetics of organic carbon mineralization and methane formation in marine sediments (Aarhus Bay, Denmark). *Geochim. Cosmochim. Acta* **252**, 159–178.

Deusner C., Holler T., Arnold G. L., Bernasconi S. M., Formolo M. J. and Brunner B. (2014) Sulfur and oxygen isotope fractionation during sulfate reduction coupled to anaerobic oxidation of methane is dependent on methane concentration. *Earth Planet. Sci. Lett.* **399**, 61–73.

Egger M., Hagens M., Sapart C. J., Dijkstra N., van Helmond N. A., Mogollón J. M., Risgaard-Petersen N., van der Veen C., Kasten S. and Riedinger N. (2017) Iron oxide reduction in methane-rich deep Baltic Sea sediments. *Geochim. Cosmochim. Acta* **207**, 256–276.

Egger M., Riedinger N., Mogollón J. M. and Jørgensen B. B. (2018) Global diffusive fluxes of methane in marine sediments. *Nat. Geosci.* **11**, 421–425.

Feng D., Peng Y., Bao H., Peckmann J., Roberts H. H. and Chen D. (2016) A carbonate-based proxy for sulfate-driven anaerobic oxidation of methane. *Geology* **44**, 999–1002.

Fike D. A., Bradley A. S. and Rose C. V. (2015) Rethinking the ancient sulfur cycle. *Annu. Rev. Earth Pl. Sc.* **43**, 593–622.

Findlay A. J., Gartman A., MacDonald D. J., Hanson T. E., Shaw T. J. and Luther G. W. (2014) Distribution and size fractionation of elemental sulfur in aqueous environments: the Chesapeake Bay and Mid-Atlantic Ridge. *Geochim. Cosmochim. Acta* **142**, 334–348.

Findlay A. J., Pellerin A., Laufer K. and Jørgensen B. B. (2020) Quantification of sulphide oxidation rates in marine sediment. *Geochim. Cosmochim. Acta* **280**, 441–452.

Fischer D., Sahling H., Nöthen K., Bohrmann G., Zabel M. and Kasten S. (2012) Interaction between hydrocarbon seepage, chemosynthetic communities, and bottom water redox at cold seeps of the Makran accretionary prism: insights from habitat-specific pore water sampling and modeling. *Biogeosciences* **9**, 2013–2031.

Flury S., Røy H., Dale A. W., Fossing H., Tóth Z., Spiess V., Jensen J. B. and Jørgensen B. B. (2016) Controls on subsurface methane fluxes and shallow gas formation in Baltic Sea sediment (Aarhus Bay, Denmark). *Geochim. Cosmochim. Acta* **188**, 297–309.

Formolo M. J. and Lyons T. W. (2013) Sulfur biogeochemistry of cold seeps in the Green Canyon region of the Gulf of Mexico. *Geochim. Cosmochim. Acta* **119**, 264–285.

Fossing H., Ferdelman T. G. and Berg P. (2000) Sulfate reduction and methane oxidation in continental margin sediments influenced by irrigation (South-East Atlantic off Namibia). *Geochim. Cosmochim. Acta* **64**, 897–910.

Fossing H. and Jørgensen B. B. (1989) Measurement of bacterial sulfate reduction in sediments: evaluation of a single-step chromium reduction method. *Biogeochemistry* **8**, 205–222.

Fossing H. and Jørgensen B. B. (1990) Isotope exchange reactions with radiolabeled sulfur compounds in anoxic seawater. *Biogeochemistry* **9**, 223–245.

Fossing H., Thode-Andersen S. and Jørgensen B. B. (1992) Sulfur isotope exchange between ^{35}S-labeled inorganic sulfur compounds in anoxic marine sediments. *Mar. Chem.* **38**, 117–132.

Fotherby A., Bradbury H. J., Antler G., Sun X., Druhan J. L. and Turchyn A. V. (2021) Modelling the effects of non-steady state transport dynamics on the sulfur and oxygen isotope composition of sulfate in sedimentary pore fluids. *Front. Earth Sci.* **8** 587085.

Fry B., Cox J., Gest H. and Hayes J. (1986) Discrimination between ^{34}S and ^{32}S during bacterial metabolism of inorganic sulfur compounds. *J. Bacteriol.* **165**, 328–330.

Fu Y., von Dobeneck T., Franke C., Heslop D. and Kasten S. (2008) Rock magnetic identification and geochemical process models of greigite formation in Quaternary marine sediments from the Gulf of Mexico (IODP Hole U1319A). *Earth Planet. Sci. Lett.* **275**, 233–245.

Glombitza C., Egger M., Røy H. and Jørgensen B. B. (2019) Controls on volatile fatty acid concentrations in marine sediments (Baltic Sea). *Geochim. Cosmochim. Acta* **258**, 226–241.

Goldhaber M. B. and Kaplan I. R. (1980) Mechanisms of sulfur incorporation and isotope fractionation during early diagenesis in sediments of the gulf of California. *Mar. Chem.* **9**, 95–143.

Gomes M. L. and Hurtgen M. T. (2015) Sulfur isotope fractionation in modern euxinic systems: Implications for paleoenvironmental reconstructions of paired sulfate–sulfide isotope records. *Geochim. Cosmochim. Acta* **157**, 39–55.

Gong S., Peng Y., Bao H., Feng D., Cao X., Crockford P. W. and Chen D. (2018) Triple sulfur isotope relationships during sulfate-driven anaerobic oxidation of methane. *Earth Planet. Sci. Lett.* **504**, 13–20.

Hardisty D. S., Lyons T. W., Riedinger N., Isson T. T., Owens J. D., Aller R. C., Rye D. M., Planavsky N. J., Reinhard C. T., Gill B. C., Masterson A. L., Asael D. and Johnston D. T. (2018) An evaluation of sedimentary molybdenum and iron as proxies for pore fluid paleoredox conditions. *Am. J. Sci.* **318**, 527–556.

Henkel S., Mogollón J. M., Nöthen K., Franke C., Bogus K., Robin E., Bahr A., Blumenberg M., Pape T., Seifert R., März C., de Lange G. J. and Kasten S. (2012) Diagenetic barium cycling in Black Sea sediments – a case study for anoxic marine environments. *Geochim. Cosmochim. Acta* **88**, 88–105.

Hensen C., Zabel M., Pfeifer K., Schwenk T., Kasten S., Riedinger N., Schulz H. D. and Boetius A. (2003) Control of sulfate pore-water profiles by sedimentary events and the significance of anaerobic oxidation of methane for the burial of sulfur in marine sediments. *Geochim. Cosmochim. Acta* **67**, 2631–2647.

Hermans M., Lenstra W. K., Hidalgo-Martinez S., van Helmond N. A. G. M., Witbaard R., Meysman F. J. R., Gonzalez S. and Slomp C. P. (2019) Abundance and biogeochemical impact of cable bacteria in Baltic Sea sediments. *Environ. Sci. Technol.* **53**, 7494–7503.

Hilligsøe K. M., Jensen J. B., Ferdelman T. G., Fossing H., Lapham L., Røy H. and Jørgensen B. B. (2018) Methane fluxes in marine sediments quantified through core analyses and seismo-acoustic mapping (Bornholm Basin, Baltic Sea). *Geochim. Cosmochim. Acta* **239**, 255–274.

Hoehler T. M. and Jørgensen B. B. (2013) Microbial life under extreme energy limitation. *Nat. Rev. Microbiol.* **11**, 83–94.

Holmkvist L., Ferdelman T. G. and Jørgensen B. B. (2011) A cryptic sulfur cycle driven by iron in the methane zone of marine sediment (Aarhus Bay, Denmark). *Geochim. Cosmochim. Acta* **75**, 3581–3599.

Holmkvist L., Kamyshny, Jr., A., Bruechert V., Ferdelman T. G. and Jørgensen B. B. (2014) Sulfidization of lacustrine glacial clay upon Holocene marine transgression (Arkona Basin, Baltic Sea). *Geochim. Cosmochim. Acta* **142**, 75–94.

Iversen N. and Jørgensen B. B. (1993) Diffusion coefficients of sulfate and methane in marine sediments: Influence of porosity. *Geochim. Cosmochim. Acta* **57**, 571–578.

Jensen J. B., Moros M., Endler R. and Members I. E. (2017) The Bornholm Basin, southern Scandinavia: a complex history from

Late Cretaceous structural developments to recent sedimentation. *Boreas* **46**, 3–17.

Jin Q. and Bethke C. M. (2009) Cellular energy conservation and the rate of microbial sulfate reduction. *Geology* **37**, 1027–1030.

Jørgensen B. B. (1978) A comparison of methods for the quantification of bacterial sulfate reduction in coastal marine sediments. *Geomicrobiol. J.* **1**, 29–47.

Jørgensen B. B. (1979) A theoretical model of the stable sulfur isotope distribution in marine sediments. *Geochim. Cosmochim. Acta* **43**, 363–374.

Jørgensen B. B. (1982) Mineralization of organic matter in the sea bed—the role of sulphate reduction. *Nature* **296**, 643–645.

Jørgensen B. B., Beulig F., Egger M., Petro C., Scholze C. and Røy H. (2019a) Organoclastic sulfate reduction in the sulfate-methane transition of marine sediments. *Geochim. Cosmochim. Acta* **254**, 231–245.

Jørgensen B. B., Böttcher M. E., Lüschen H., Neretin L. N. and Volkov I. I. (2004) Anaerobic methane oxidation and a deep H_2S sink generate isotopically heavy sulfides in Black Sea sediments. *Geochim. Cosmochim. Acta* **68**, 2095–2118.

Jørgensen B. B., Findlay A. J. and Pellerin A. (2019b) The biogeochemical sulfur cycle of marine sediments. *Front. Microbiol.* **10**, 849.

Jørgensen B. B. and Kasten S. (2006) Sulfur cycling and methane oxidation. In *Marine Geochemistry* (eds. H. D. Schulz and M. Zabel). Springer Berlin Heidelberg, Berlin, Heidelberg, pp. 271–309.

Jørgensen B. B. and Nelson D. C. (2004) Sulfide oxidation in marine sediments: Geochemistry meets microbiology. In *Sulfur Biogeochemistry - Past and Present* (eds. J. P. Amend, K. J. Edwards and T. W. Lyons). Geological Society of America, Boulder, Colorado, pp. 63–82.

Jørgensen B. B. and Parkes R. J. (2010) Role of sulfate reduction and methane production by organic carbon degradation in eutrophic fjord sediments (Limfjorden, Denmark). *Limnol. Oceanogr.* **55**, 1338–1352.

Jørgensen B. B., Weber A. and Zopfi J. (2001) Sulfate reduction and anaerobic methane oxidation in Black Sea sediments. *Deep-Sea Res. Pt. I* **48**, 2097–2120.

Kaplan I. R., Emery K. O. and Rittenbebg S. C. (1963) The distribution and isotopic abundance of sulphur in recent marine sediments off southern California. *Geochim. Cosmochim. Acta* **27**, 297–331.

Kaplan I. R. and Rittenberg S. C. (1964) Microbiological fractionation of sulphur isotopes. *Microbiology* **34**, 195–212.

Kasten S., Freudenthal T., Gingele F. X. and Schulz H. D. (1998) Simultaneous formation of iron-rich layers at different redox boundaries in sediments of the Amazon deep-sea fan. *Geochim. Cosmochim. Acta* **62**, 2253–2264.

Knittel K. and Boetius A. (2009) Anaerobic oxidation of methane: progress with an unknown process. *Annu. Rev. Microbiol.* **63**, 311–334.

Lang X., Tang W., Ma H. and Shen B. (2020) Local environmental variation obscures the interpretation of pyrite sulfur isotope records. *Earth Planet. Sci. Lett.* **533** 116056.

Leavitt W. D., Halevy I., Bradley A. S. and Johnston D. T. (2013) Influence of sulfate reduction rates on the Phanerozoic sulfur isotope record. *P. Natl. Acad. Sci. USA* **110**, 11244–11249.

Leloup J., Fossing H., Kohls K., Holmkvist L., Borowski C. and Jørgensen B. B. (2009) Sulfate-reducing bacteria in marine sediment (Aarhus Bay, Denmark): abundance and diversity related to geochemical zonation. *Environ. Microbiol.* **11**, 1278–1291.

Lin Z., Sun X., Peckmann J., Lu Y., Xu L., Strauss H., Zhou H., Gong J., Lu H. and Teichert B. M. A. (2016) How sulfate-driven anaerobic oxidation of methane affects the sulfur isotopic composition of pyrite: A SIMS study from the South China Sea. *Chem. Geol.* **440**, 26–41.

Liu J., Antler G., Pellerin A., Izon G., Dohrmann I., Findlay A. J., Røy H., Ono S., Turchyn A. V., Kasten S. and Jørgensen B. B. (2021) Isotopically "heavy" pyrite in marine sediments due to high sedimentation rates and non-steady-state deposition. *Geology* **49**, 816–821.

Liu J., Pellerin A., Antler G., Kasten S., Findlay A. J., Dohrmann I., Røy H., Turchyn A. V. and Jørgensen B. B. (2020a) Early diagenesis of iron and sulfur in Bornholm Basin sediments: The role of near-surface pyrite formation. *Geochim. Cosmochim. Acta* **284**, 43–60.

Liu J., Pellerin A., Izon G., Wang J., Antler G., Liang J., Su P., Jørgensen B. B. and Ono S. (2020b) The multiple sulphur isotope fingerprint of a sub-seafloor oxidative sulphur cycle driven by iron. *Earth Planet. Sci. Lett.* **536** 116165.

Liu X., Fike D., Li A., Dong J., Xu F., Zhuang G., Rendle-Bühring R. and Wan S. (2019) Pyrite sulfur isotopes constrained by sedimentation rates: Evidence from sediments on the East China Sea inner shelf since the late Pleistocene. *Chem. Geol.* **505**, 66–75.

Martens C. S. and Berner R. A. (1977) Interstitial water chemistry of anoxic Long Island Sound sediments. 1. Dissolved gases. *Limnol. Oceanogr.* **22**, 10–25.

März C., Hoffmann J., Bleil U., De Lange G. and Kasten S. (2008) Diagenetic changes of magnetic and geochemical signals by anaerobic methane oxidation in sediments of the Zambezi deep-sea fan (SW Indian Ocean). *Mar. Geol.* **255**, 118–130.

Masterson A. L. (2016) *Multiple sulfur isotope applications in diagenetic models and geochemical proxy records* Ph.D. thesis. Harvard University.

Masterson A., Alperin M. J., Berelson W. M. and Johnston D. T. (2018) Interpreting multiple sulfur isotope signals in modern anoxic sediments using a full diagenetic model (California-Mexico margin: Alfonso Basin). *Am. J. Sci.* **318**, 459–490.

Middelburg J. J. (1991) Organic carbon, sulphur, and iron in recent semi-euxinic sediments of Kau Bay, Indonesia. *Geochim. Cosmochim. Acta* **55**, 815–828.

Millero F. J., Plese T. and Fernandez M. (1988) The dissociation of hydrogen sulfide in seawater. *Limnol. Oceanogr.* **33**, 269–274.

Mills J. V., Antler G. and Turchyn A. V. (2016) Geochemical evidence for cryptic sulfur cycling in salt marsh sediments. *Earth Planet. Sci. Lett.* **453**, 23–32.

Mogollón J. M., Dale A. W., Fossing H. and Regnier P. (2012) Timescales for the development of methanogenesis and free gas layers in recently-deposited sediments of Arkona Basin (Baltic Sea). *Biogeosciences* **9**, 1915–1933.

Moros M., Lemke W., Kuijpers A., Endler R., Jensen J. B., Bennike O. and Gingele F. (2002) Regressions and transgressions of the Baltic basin reflected by a new high-resolution deglacial and postglacial lithostratigraphy for Arkona Basin sediments (western Baltic Sea). *Boreas* **31**, 151–162.

Neretin L. N., Böttcher M. E., Jørgensen B. B., Volkov I. I., Lüschen H. and Hilgenfeldt K. (2004) Pyritization processes and greigite formation in the advancing sulfidization front in the upper Pleistocene sediments of the Black Sea. *Geochim. Cosmochim. Acta* **68**, 2081–2093.

Niewöhner C., Hensen C., Kasten S., Zabel M. and Schulz H. D. (1998) Deep sulfate reduction completely mediated by anaerobic methane oxidation in sediments of the upwelling area off Namibia. *Geochim. Cosmochim. Acta* **62**, 455–464.

Ono S., Keller N. S., Rouxel O. and Alt J. C. (2012) Sulfur-33 constraints on the origin of secondary pyrite in altered oceanic basement. *Geochim. Cosmochim. Acta* **87**, 323–340.

Ono S., Wing B., Johnston D., Farquhar J. and Rumble D. (2006) Mass-dependent fractionation of quadruple stable sulfur isotope system as a new tracer of sulfur biogeochemical cycles. *Geochim. Cosmochim. Acta* **70**, 2238–2252.

Pasquier V., Bryant R. N., Fike D. A. and Halevy I. (2021) Strong local, not global, controls on marine pyrite sulfur isotopes. *Sci. Adv.* **7**, eabb7403.

Pasquier V., Sansjofre P., Rabineau M., Revillon S., Houghton J. and Fike D. A. (2017) Pyrite sulfur isotopes reveal glacial–interglacial environmental changes. *P. Natl. Acad. Sci. USA* **114**, 5941–5945.

Pellerin A., Antler G., Røy H., Findlay A., Beulig F., Scholze C., Turchyn A. V. and Jørgensen B. B. (2018) The sulfur cycle below the sulfate-methane transition of marine sediments. *Geochim. Cosmochim. Acta* **239**, 74–89.

Pellerin A., Bui T. H., Rough M., Mucci A., Canfield D. E. and Wing B. A. (2015) Mass-dependent sulfur isotope fractionation during reoxidative sulfur cycling: A case study from Mangrove Lake, Bermuda. *Geochim. Cosmochim. Acta* **149**, 152–164.

Petro C., Zäncker B., Starnawski P., Jochum L. M., Ferdelman T. G., Jørgensen B. B., Røy H., Kjeldsen K. U. and Schramm A. (2019) Marine deep biosphere microbial communities assemble in near-surface sediments in Aarhus Bay. *Front. Microbiol.* **10** 758.

Piel C. (1999) *Experimental studies of sulfur isotope fractionation ($^{34}S/^{32}S$) during transport and reaction of dissolved and gaseous sulfur species* M.Sc. thesis. University of Bremen.

Raven M. R., Sessions A. L., Fischer W. W. and Adkins J. F. (2016) Sedimentary pyrite $\delta^{34}S$ differs from porewater sulfide in Santa Barbara Basin: Proposed role of organic sulfur. *Geochim. Cosmochim. Acta* **186**, 120–134.

Rickard D. and Morse J. W. (2005) Acid volatile sulfide (AVS). *Mar. Chem.* **97**, 141–197.

Riedinger N., Brunner B., Formolo M. J., Solomon E., Kasten S., Strasser M. and Ferdelman T. G. (2010) Oxidative sulfur cycling in the deep biosphere of the Nankai Trough, Japan. *Geology* **38**, 851–854.

Riedinger N., Brunner B., Krastel S., Arnold G. L., Wehrmann L. M., Formolo M. J., Beck A., Bates S. M., Henkel S. and Kasten S. (2017) Sulfur cycling in an iron oxide-dominated, dynamic marine depositional system: The Argentine continental margin. *Front. Earth Sci.* **5**, 33.

Riedinger N., Pfeifer K., Kasten S., Garming J. F. L., Vogt C. and Hensen C. (2005) Diagenetic alteration of magnetic signals by anaerobic oxidation of methane related to a change in sedimentation rate. *Geochim. Cosmochim. Acta* **69**, 4117–4126.

Roberts A. P. (2015) Magnetic mineral diagenesis. *Earth-Sci. Rev.* **151**, 1–47.

Shawar L., Halevy I., Said-Ahmad W., Feinstein S., Boyko V., Kamyshny A. and Amrani A. (2018) Dynamics of pyrite formation and organic matter sulfurization in organic-rich carbonate sediments. *Geochim. Cosmochim. Acta* **241**, 219–239.

Sim M. S., Bosak T. and Ono S. (2011a) Large sulfur isotope fractionation does not require disproportionation. *Science* **333**, 74–77.

Sim M. S., Ono S., Donovan K., Templer S. P. and Bosak T. (2011b) Effect of electron donors on the fractionation of sulfur isotopes by a marine Desulfovibrio sp. *Geochim. Cosmochim. Acta* **75**, 4244–4259.

Sohlenius G., Emeis K. C., Andrén E., Andrén T. and Kohly A. (2001) Development of anoxia during the Holocene fresh–brackish water transition in the Baltic Sea. *Mar. Geol.* **177**, 221–242.

Strauss H. (1997) The isotopic composition of sedimentary sulfur through time. *Palaeogeogr., Palaeoclimatol., Palaeoecol.* **132**, 97–118.

Strauss H., Bast R., Cording A., Diekrup D., Fugmann A., Garbe-Schönberg D., Lutter A., Oeser M., Rabe K., Reinke D., Teichert B. M. A. and Westernströer U. (2012) Sulphur diagenesis in the sediments of the Kiel Bight, SW Baltic Sea, as reflected by multiple stable sulphur isotopes. *Isotopes Environ. Health Stud.* **48**, 166–179.

Turchyn A. V., Antler G., Byrne D., Miller M. and Hodell D. A. (2016) Microbial sulfur metabolism evidenced from pore fluid isotope geochemistry at Site U1385. *Global Planet. Change* **141**, 82–90.

Turchyn A. V., Sivan O. and Schrag D. P. (2006) Oxygen isotopic composition of sulfate in deep sea pore fluid: evidence for rapid sulfur cycling. *Geobiology* **4**, 191–201.

Wijsman J. W. M., Middelburg J. J., Herman P. M. J., Böttcher M. E. and Heip C. H. R. (2001) Sulfur and iron speciation in surface sediments along the northwestern margin of the Black Sea. *Mar. Chem.* **74**, 261–278.

Wilkin R. T. and Barnes H. L. (1996) Pyrite formation by reactions of iron monosulfides with dissolved inorganic and organic sulfur species. *Geochim. Cosmochim. Acta* **60**, 4167–4179.

Wing B. A. and Halevy I. (2014) Intracellular metabolite levels shape sulfur isotope fractionation during microbial sulfate respiration. *P. Natl. Acad. Sci. USA* **111**, 18116–18125.

Wortmann U. G., Bernasconi S. M. and Böttcher M. E. (2001) Hypersulfidic deep biosphere indicates extreme sulfur isotope fractionation during single-step microbial sulfate reduction. *Geology* **29**, 647–650.

Wortmann U. G. and Chernyavsky B. M. (2011) The significance of isotope specific diffusion coefficients for reaction-transport models of sulfate reduction in marine sediments. *Geochim. Cosmochim. Acta* **75**, 3046–3056.

Zerkle A. L., Farquhar J., Johnston D. T., Cox R. P. and Canfield D. E. (2009) Fractionation of multiple sulfur isotopes during phototrophic oxidation of sulfide and elemental sulfur by a green sulfur bacterium. *Geochim. Cosmochim. Acta* **73**, 291–306.

Associate editor: Filip Meysman